

**THE UNIVERSITY OF CALGARY**

**Modeling Observed X-ray Pulsar Profiles**

**by**

**Lan Li**

**A THESIS**

**SUBMITTED TO THE FACULTY OF GRADUATE STUDIES  
IN PARTIAL FULFILLMENT OF THE REQUIREMENTS FOR THE  
DEGREE OF MASTER OF SCIENCE**

**DEPARTMENT OF PHYSICS AND ASTRONOMY**

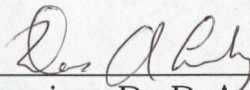
**CALGARY, ALBERTA**

**MAY, 1995**

**© Lan Li 1995**

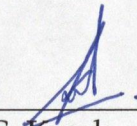
THE UNIVERSITY OF CALGARY  
FACULTY OF GRADUATE STUDIES

The undersigned certify that they have read, and recommend to the faculty of Graduate Studies for acceptance, a thesis entitled "Modeling Observed X-ray Pulsar Profiles" submitted by Lan Li in partial fulfillment of the requirements for the degree of Master of Science.



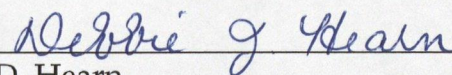
---

Supervisor, Dr. D. A. Leahy  
Department of Physics and Astronomy



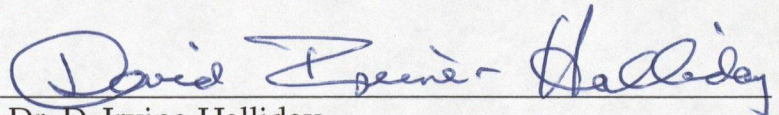
---

Dr. S. Kwok  
Department of Physics and Astronomy



---

Dr. D. Hearn  
Department of Physics and Astronomy



---

Dr. D. Irvine-Halliday  
Electrical and Computer Engineering Department

1 May 95

Date

## ABSTRACT

The purpose of this work was to generalize pulse shape modeling to include the effect of light bending due to general relativity. A simple analytical formula was found to accurately describe the light bending effect, and was incorporated into the emission model for calculation of the pulse shapes from rotating accreting neutron stars. Least square fittings were performed to a subset of pulsars studied by Leahy, 1991<sup>[2]</sup>. The fittings with light bending showed significant improvement over the fittings without light bending, and the resulting derived emission region geometry gave narrower rings, as expected on theoretical grounds. The model was also applied to the luminosity dependent pulse profile of EXO2030+375. The relation between the luminosity and the properties of the emissions rings were studied. The lack of success of the model on EXO2030+375 was probably caused by the model being too simple geometrically. Future improvements to the model were discussed.

## ACKNOWLEDGMENTS

I would like to acknowledge the following people for their contributions to this thesis. My supervisor, Dr. D. A. Leahy, is thoroughly involved in this thesis. Without his guidance, his suggestions, and his patience to answer my various questions, this thesis would not exist. I appreciate the many constructive opinions and words of encouragement from my committee members: Dr. S. Kwok, Dr. D. Hearn, and Dr. D. Irvine-Halliday. I also appreciate the work of Dr. D. S. Phillips, for his valuable suggestions to speed up my FORTRAN program; Mr. Ken Lai, for maintaining an excellent computing facility; Dr. Kevin Volk and Dr. Richard Szczerba for their friendships and countless helps.

## TABLE OF CONTENTS

APPROVAL PAGE	ii
ABSTRACT	iii
ACKNOWLEDGMENTS	iv
TABLE OF CONTENTS	v
LIST OF TABLES	viii
LIST OF FIGURES	ix
CHAPTER 1	
INTRODUCTION	1
1 .1 Introduction to X-ray Pulsars .....	1
1 .2 Thesis Subject and Outline .....	3
CHAPTER 2	
THE EMISSION MODEL	5
2 .1 Emission Region And Radiation Pattern .....	5
2 .2 Geometry of the Model .....	8
2 .3 The Integration .....	10
2 .4 Model Fits to the Observed X-ray Pulse Profiles .....	13
2 .5 The Fitting Program .....	15
CHAPTER 3	
GRAVITATIONAL LIGHT BENDING	17
3 .1 Introduction .....	17
3 .2 The Light Bending Equation .....	18
3 .3 The Linear Fittings to the Light Bending Equation .....	19

## CHAPTER 4

### Fitting of the pulsar Profile:

<b>The Effects of Relativistic Light-Bending</b>	<b>25</b>
4.1 Introduction .....	25
4.2 The Observations of X-ray Pulsars .....	26
4.3 The Model Fits to the Pulsar Profiles .....	28
4.4 The Fitted Profiles for X-ray Pulsars .....	30
4.5 Conclusion .....	32

## CHAPTER 5

### EXO 2030+375:

<b>The Luminosity Dependence of Pulse Profile</b>	<b>40</b>
5.1 Introduction .....	40
5.2 The Observed Pulse Profiles .....	42
5.3 Model Assumptions and Pulse Profile Fittings .....	45
5.4 Fan Beam Radiation Pattern .....	57
5.5 Conclusion .....	59

## CHAPTER 6

<b>CONCLUSION</b>	<b>60</b>
6.1 Summary .....	60
6.2 Future Work .....	61

## Appendix

<b>The Analytical and Numerical Integrations in the Fitting Program</b>	<b>63</b>
1. Structure of the fitting program .....	63
2. Overview of the equations .....	65

3 . The analytical formulae for the no light bending model . . . . .	67
4 . The numerical integration for the light bending model . . . . .	68

**REFERENCES**

**71**

## LIST OF TABLES

Table 2-1	Models and their parameter numbers .....	15
Table 3-1	Fitted slope (a) and intercept (b) for different $r_0$ .....	21
Table 4-1	X-ray Pulsars .....	27
Table 4-2	Pulse profile model parameters .....	29
Table 4-3	Comparison of the two models .....	31
Table 5-1	Model parameters for EXO 2030+375 .....	47
Table 5-2	Luminosities and emission region sizes of EXO 2030+375.....	55

## LIST OF FIGURES

- Fig 2-1 Schematic diagram of the mass change possibilities: (a) due to a wind from the companion star, or (b) due to Roche lobe overflow, through the inner Lagrangian point. . . . . 5
- Fig 2-2 Interaction of an accretion disk with the magnetosphere. The matter is channeled down the field lines to the polar cap regions, where it produces X-rays. . . . . 6
- Fig 2-3 Possible longitudinal geometry of the emission region: (a) Pillbox shape, arising from radiation or collisionless shock deceleration, gives a fan beam pattern, radiation being emitted sideways. (b) Plane parallel atmosphere, which does not stick out above the surface and arises if Coulomb and nuclear particle encounters produce the deceleration. This produce a pencil beam, radiation escaping upwards. . . . . 7
- Fig 2-4 The geometry of the emission rings showing the definitions of various angles. . . . . 8
- Fig 2-5 The relation between the observer direction and the neutron star  $z'$  axis showing definitions of associated angles. . . . . 14
- Fig 3-1 Geometry of the light bending, showing coordinates of emission point Q ( $r_0, \theta'', \phi''$ ) and the observer point P ( $r, \theta_1, \phi_1$ ). . . . . 18
- Fig 3-2 Linear fittings of the light bending formula (equation 2-5) for two typical

values of neutron star radius: a)  $r_0=2.4184$ , for most neutron stars; b)  $r_0=4.4008$ , for Her X-1. The data points are numerical calculations from equation (2-5)..... 22

Fig 3-3 a) Fitted relation between slope and  $r_0$  . b) Fitted relation between intercept and  $r_0$  ..... 23

Fig 3-4 When , the plot of  $\cos\theta_0'$  .vs.  $\cos\theta$  is obviously curved, the data points deviate from a straight line. Linear fitting is not suitable for the full range of  $\cos\theta'$ , but still perfect in a smaller range: [0.4, 1] for  $r_0=1.6$ ; [0.3, 1] for  $r_0=1.8$ . ..... 24

Fig 4-1 Pulsar Profiles for 4U0115+63. (a) Profile for no light-bending model, SSQ=1.499. (b) Profile for light-bending model, SSQ=1.331. .... 33

Fig 4-2 Pulse profiles for Cen X-3. (a) Profile for no light-bending model, SSQ=0.342. (b) Profile for light-bending model, SSQ=0.164. .... 34

Fig 4-3 Pulse profiles for 4U1626-67. (a) Profile for no light-bending model, SSQ=0.668. (b) Profile for light-bending model, SSQ=0.664. .... 35

Fig 4-4 Pulse profiles for 4U1258-62. (a) Profile for no light-bending model, SSQ=0.029. (b) Profile for light-bending model, SSQ=0.023. .... 36

Fig 4-5 Pulse profiles for 4U0900-40. (a) Profile for no light-bending model, SSQ=0.339. (b) Profile for light-bending model, SSQ=0.080. .... 37

Fig 4-6	Pulse profiles for 4U1118-61. (a) Profile for no light-bending model, SSQ=0.213. (b) Profile for light-bending model, SSQ=0.049 . . . . .	38
Fig 4-7	Pulse profiles for GPS1722-36. (a) Profile for no light-bending model, SSQ=4.249. (b) Profile for light-bending model, SSQ=4.210. . . . .	39
Fig 5-1	The observed light curves of the first 5 days. 1.5 cycles are shown. The light curves have been aligned in phase so that the sharp notch visible of the main broad peak is centered on $\Phi = 0.0$ . . . . .	43
Fig 5-2	The observed light curves of the last 5 days. . . . .	44
Fig 5-3	Pulse profile for May 18 and May 23 after $\theta_m, \theta_r, \theta_o$ are fixed. The first five and last five data points are ignored in the fitting. . . . .	49
Fig 5-4	Pulse profile for May 29 and June 5 after $\theta_m, \theta_r, \theta_o$ are fixed. The first five and last five data points are ignored in the fitting. . . . .	50
Fig 5-5	Pulse profile for June 14 and June 21 after $\theta_m, \theta_r, \theta_o$ are fixed. The first five and last five data points are ignored in the fitting. . . . .	51
Fig 5-6	Pulse profile for June 27 and July 10 after $\theta_m, \theta_r, \theta_o$ are fixed. The first five and last five data points are ignored in the fitting. . . . .	52
Fig 5-7	Pulse profile for July 25 and Aug. 13 after $\theta_m, \theta_r, \theta_o$ are fixed. The first five and last five data points are ignored in the fitting. . . . .	53

Fig 5-8 Emission ring angles .vs. dates for both rings. Luminosity is decreasing with time. No regularity is shown on the positions and widths of the rings. .... 54

Fig 5-9 Luminosity .vs.  $\Omega$ . The equation for the straight line is:  $L = 0.401 \times 10^{38} \Omega - 0.366 \times 10^{38}$ . Although the four circled points scatter quite far away from the line, the other six points do follow the trend of the line, displaying an approximate proportional relation between luminosity and emission region size, which is consistent with the model assumptions. .... 56

Fig 5-10 Possible transverse geometries of the emission region at polar cap: (a) Filled funnel. (b) Hollow sectional funnel. (c) Pancaked. (d) Spaghettis. (Adopted from Mészáros, P., 1984)<sup>[6]</sup>. .... 58

Fig 6-1 A simple geometry approximation for fan beam model: Two offset thin columns, with different height:  $h_1, h_2$ . .... 61

Fig A-2 Structure of the fitting program .... 64

Fig A-3 Equation overview for the Geometric Model. .... 66

## CHAPTER 1

### INTRODUCTION

#### 1.1 Introduction to X-ray Pulsars

Under current theories, X-ray pulsars are assumed to be rotating magnetic neutron stars. Their cores are composed primarily of neutrons, as are expected to occur when the mean density is in the range  $10^{13} - 10^{15} \text{ g/cm}^3$ .

The concept of neutron star was introduced into the scientific world about sixty years ago by Baade and Zwicky as one of the possible end-points of stellar evolution. They pointed out that the enormous energy release of supernova explosions could transit ordinary stars to compact stars, which are at very high density, small radius, and much more gravitationally bound than ordinary stars, and as a result neutron stars could be formed. Despite extensive theoretical works on neutron star structure and some suggestions as possible X-ray sources since then, the neutron star was observationally discovered only in 1968 as the radio pulsar. Just previous to that Shklovsky opened a new door, suggesting that X-ray sources could be binaries consisting of neutron stars accreting matter from companion stars. This idea was confirmed by the discovery of binary X-ray pulsars Cen X-3 and Her X-1; they are neutron stars spinning with periods of 4.87s and 1.24s and orbiting around companion stars with periods of 2.1d and 1.7d, respectively.

In the last decade since the discovery of binary X-ray pulsars, much progress has been made in understanding the nature of bright X-ray sources which are powered by the accretion of matter by neutron stars. About thirty of them have been found to pulsate, while the orbital periods have been measured for about twenty sources. Neither pulsation nor orbital motion has yet been observed for many bright X-ray sources, but they are considered to be mostly binaries

containing neutron stars. About thirty of them are transient sources which show long-term variabilities, and about thirty sources occasionally emit X-ray bursts, enhanced X-ray emission lasting for seconds to minutes. There are other classes of X-ray binaries which consist of white dwarfs or black holes, and some of them may be confused with those containing neutron stars.

Binary X-ray sources derive their energy from gravitational potential energy released when matter is accreted onto a compact object. According to the standard accretion picture, matter from a companion star falls onto the magnetic poles of a rotating neutron star, converting its gravitational energy into radiation on the surface of the star. Pulsations are observed due to the emission region on the surface of the neutron star, where the accreting matter releases its energy, rotating in and out of the field of view. The energy released when a proton is lowered onto the surface of a neutron star, of mass 1.4 solar mass and radius 10 km, is 166 Mev. Thus relatively modest rates of mass transfer onto a compact object can generate large X-ray luminosities. A companion star is generally necessary to provide the matter.

Matter can be transferred to neutron star from its binary companion in at least two ways: by a stellar wind or by Roche or tidal lobe overflow. In the case of accretion from a wind, some of the plasma lost by the companion star is drawn toward the neutron star by the latter's gravity, cools, and is captured. The wind capture radius is generally smaller than the separation between the two stars, but larger than the radius of the neutron star's magnetosphere. Plasma captured from a wind has some angular momentum with respect to the neutron star, but may not have enough to form a Keplerian accretion disk. In the case of Roche or tidal lobe overflow, relatively cold plasma flows slowly over the gravitational saddle point between the two stars and is immediately captured by the neutron star. Plasma captured in this way has a larger angular momentum with respect

to the neutron star and will form an accretion disk. The accretion disk in its standard form (e.g. Pringle & Rees 1972)<sup>[1]</sup> is a geometrically thin, optically thick structure which has its dynamics dominated primarily by the Keplerian motion of gas around the central object. In such a disk, the gravitational attraction of the neutron star is canceled by centrifugal force, and the plasma spirals slowly inward as its angular momentum is transported outward by shear stresses. In most X-ray binaries, mass is transferred by both of these two processes.

The binary X-ray pulsars exhibit a wide variety of pulse shapes, from simple nearly sinusoidal profiles to complex multi-peaked profiles. For some pulsars the pulse shapes are strongly dependent on energy, for others the shapes are nearly independent of energy. There are many factors which govern the observed pulse shape: the geometry of the emission region; the viewing angle to the observer; and the magnetic field strength are three.

A large number of theoretical investigations have been performed in order to model the spectra and the pulse profiles as well as the gas dynamical structure of the accretion flow itself. The asymmetry of the pulses, however, has been largely neglected in the models so far, although it is an obvious phenomenon apparent in almost all observed pulsars. Only recently, Leahy (1991)<sup>[2]</sup> has made an attempt to fit the observed pulse profiles to the results obtained from a simple emission model.

## **1.2 Thesis Subject and Outline**

The subject of this thesis is to fit the observed pulse profiles to a simple emission model, and analyze the properties of the fittings.

Chapter 2 describes the radiation pattern for emission, and the geometry of the

model. Chapter 3 gives a simple analytical formula for the gravitational light bending effect, and makes it possible to be incorporated into the model fitting. Chapter 4 shows the fittings of the light bending model and compares them with the fits of the no light bending model. Chapter 5 applies the model to a transient X-ray pulsar EXO 2030+375, trying to explain the luminosity dependence of the pulse profile. Conclusions of this thesis and future work are discussed in Chapter 6. Some details of the fitting program are described in the Appendix.

## CHAPTER 2

### THE EMISSION MODEL

#### 2.1 Emission Region And Radiation Pattern

The basic model used to interpret pulsating X-ray sources has remained essentially unchanged since its inception (Pringle & Rees, 1972<sup>[1]</sup>; Davison & Ostriker, 1973<sup>[3]</sup>; Lamb et al., 1973<sup>[4]</sup>). In the usual picture, matter is assumed to be lost from the companion star either via a stellar wind or via slow leakage through the inner lagrangian point. (see Fig 2-1)

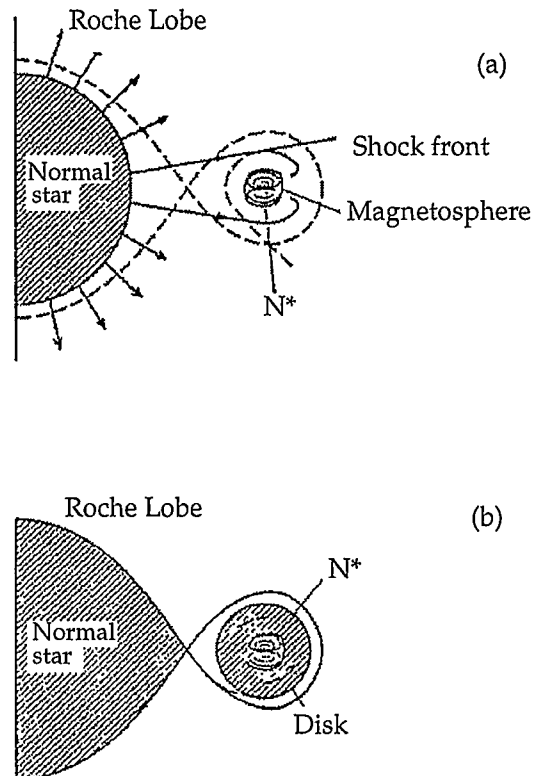


*Fig 2-1* Schematic diagram of the mass change possibilities: (a) due to a wind from the companion star, or (b) due to Roche lobe overflow, through the inner Lagrangian point.

Ghosh & Lamb (1979)<sup>[5]</sup> described the accretion process for a highly magnetized neutron star. As the matter gets closer to the neutron star, magnetic forces become important. They assumed that the magnetic field of the neutron star rapidly threads the accreting plasma and that it enforces corotation inside the surface where the flow velocity becomes sub-Alfvénic in the stellar magnetic field. They called this surface the “Alfvén Surface” and argued that it represents the effective extent of the neutron star magnetosphere. The matter should be ionized and highly conducting before reaching the Alfvén surface. At the Alfvén radius, where the magnetic pressure balances the ram pressure of the freely infalling matter, the accreting matter is stopped and then it threads the magnetic lines. After threading, the matter follows the field lines to the neutron star surface. It arrives on a region the shape of a ring around each of the magnetic poles for the case of dipole field geometry. (see Fig 2-2).

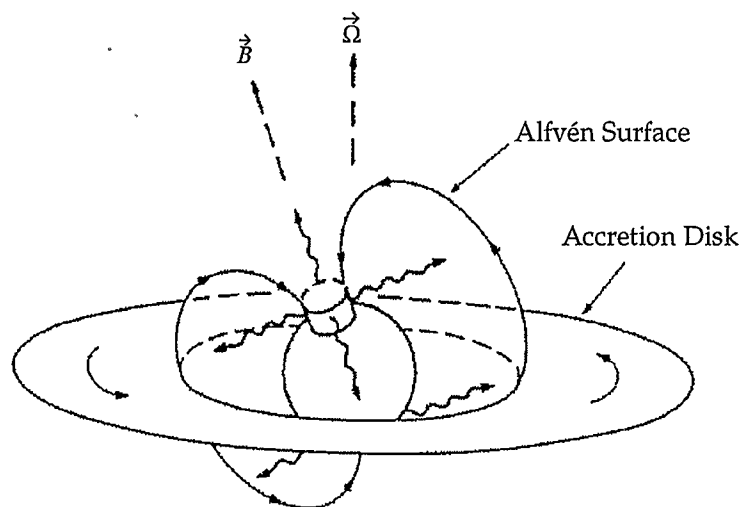


*Fig 2-2* Interaction of an accretion disk with the magnetosphere. The matter is channeled down the field lines to the polar cap regions, where it produces X-rays.

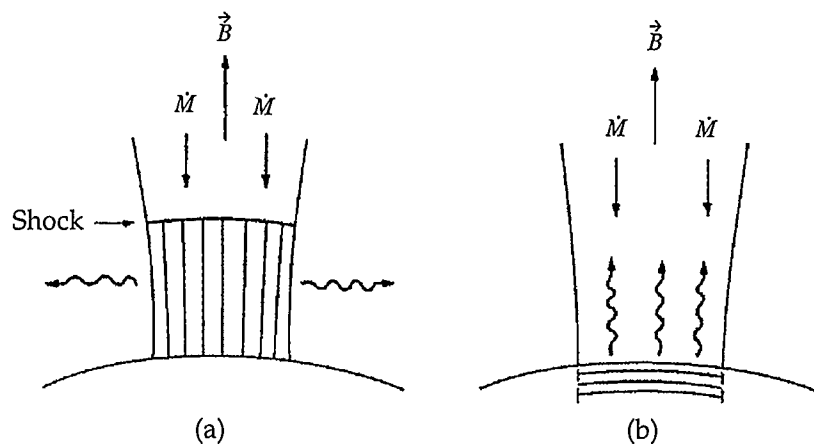


*Fig 2-3* Possible longitudinal geometry of the emission region: (a) Pillbox shape, arising from radiation or collisionless shock deceleration, gives a fan beam pattern, radiation being emitted sideways. (b) Plane parallel atmosphere, which does not stick out above the surface and arises if Coulomb and nuclear particle encounters produce the deceleration. This produce a pencil beam, radiation escaping upwards.

(Fig 2-1 — Fig 2-3 are adopted from Mészáros, P., 1984)<sup>[6]</sup>

How this occurs exactly is one of the key factors determining the vertical structure of the emission region and thus the radiation pattern. Whether the plasma effects will induce a collisionless shock above the surface or not is the main uncertainty. In the shock case, the standoff distance is a fraction of the stellar radius, so the emitting postshock region is a cylinder sticking out above the surface, and there is a large, if not predominant, component of emission from the sides, in a fan beam pattern (The flux:  $I(\theta) = I \sin^n(\theta)$ ). In the absence of a shock, for  $L \leq 10^{37}$  ergs/s, the deceleration occurs via multiple coulomb encounters or nuclear collisions with the atmospheric particles, occurring in the denser part of the atmosphere. The atmosphere is a plane parallel section of the

polar cap, which does not significantly stick out, emitting upwards in a pencil beam (The flux:  $I(\theta) = I \cos^n(\theta)$ ). (see Fig 2-3). Mészáros & Nagel (1985)<sup>[7]</sup> performed the calculations on both cases, indicated that the slab model (pencil beam) are in better general agreement with the observations than column models (the fan beam). So, the pencil beam pattern will be considered in this thesis.

## 2.2 Geometry of the Model

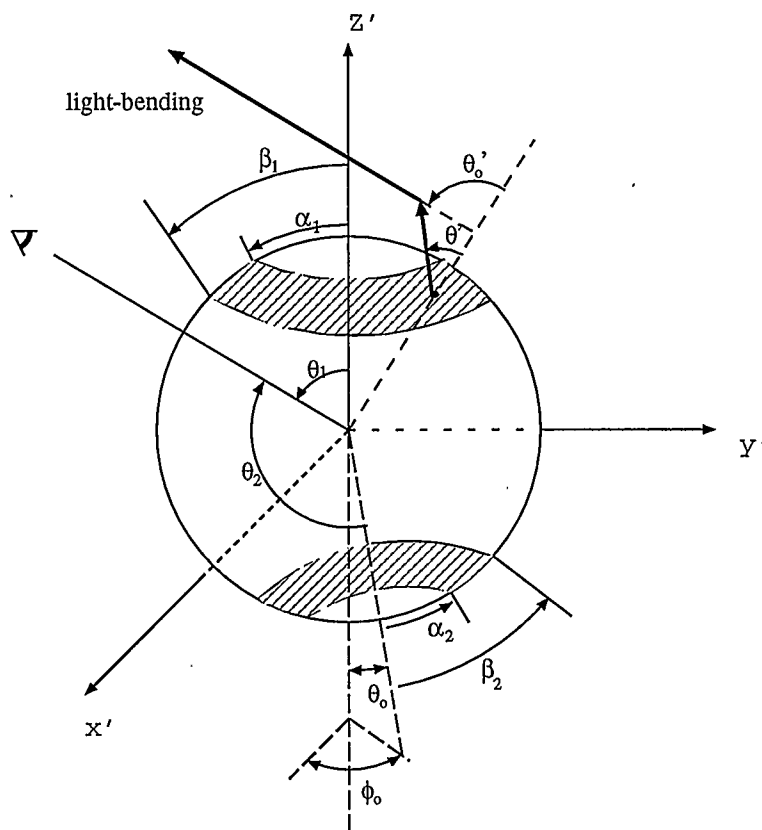


*Fig 2-4* The geometry of the emission rings showing the definitions of various angles.

The geometry of the emission is shown in Fig 2-4. This model assumes two emission rings offset by an angle  $\theta_0$  on the surface of the neutron star, each centered about an axis of the neutron star. Each ring is taken to have uniform emission from  $\theta'' = \alpha_1$  (or  $\alpha_2$ ) to  $\theta'' = \beta_1$  (or  $\beta_2$ ) with  $\theta''$  the angle from each axis. One axis is offset by an angle  $\theta_0$  from the first (taken to lie along the  $z'$  axis) and the azimuthal location of the second axis is specified by  $\phi_0$ . The first axis is also called the north magnetic axis.

The accretion rate is taken to be constant in time. The flux,  $I(\theta') \cos\theta'$  is taken to be one of the two analytic functions which are simple approximations (Leahy 1990)<sup>[8]</sup> to the theoretical calculations of Mészáros & Nagel (1985)<sup>[7]</sup> for emission by a slab of magnetized plasma:

$$I(\theta') \cos\theta' = A \cos^2\theta' \quad (2-1)$$

$$I(\theta') \cos\theta' = A \cos^4\theta' \quad (2-2)$$

Here  $\theta'$  is called the emission angle. It is the angle of the emission light with respect to the local normal of the neutron star surface. The light will reach the observer at angle  $\theta_0'$  due to light bending (see Fig 2-4).

The angular distribution of the flux from the surface the neutron star  $f(\theta_1, \phi_1)$  is given by the integration of  $I(\theta') \cos(\theta')$  over the emission region:

$$f(\theta_1, \phi_1) = \int d\Omega'' I(\theta') \cos\theta' \quad (2-3)$$

Where  $d\Omega'' = \sin\theta'' d\theta'' d\phi''$ . Here  $\theta''$  and  $\phi''$  are the spherical polar coordinates of frame  $x'y'z'$  (with  $z'$  along the magnetic axis).

To do this integration, we need to know the dependence of  $I(\theta')$   $\cos\theta'$  on  $\theta''$  and  $\phi''$ . This dependence can be found through the dependence of  $\cos\theta_0'$  on  $\theta''$  and  $\phi''$  (equation 2-4), and the light-bending relation between  $\theta_0'$  and  $\theta'$  (equation 2-5).

$$\cos\theta_0' = \cos\theta_1 \cos\theta'' + \sin\theta_1 \sin\theta'' \cos(\phi'' - \phi_1) \quad (2-4)$$

$$\theta_0'(r, r_0, \mu) = b \int_{r_0}^r \frac{1}{x} \left[ x^2 - b^2 \left( 1 - \frac{1}{x} \right) \right]^{-1/2} dx \quad (2-5)$$

Where:

$$\mu = \cos\theta'$$

$$b = \frac{r_0}{A_0} (1 - \mu^2)^{1/2}$$

$$A_0 = \left( 1 - \frac{1}{r_0} \right)^{1/2}$$

$$r_0 = \frac{Rc^2}{2GM} \quad (\text{Neutron star radius in Schwarzschild units})$$

Equation (2-5) is a formula for general relativistic light bending (Riffert & Mészáros, 1988)<sup>[9]</sup>. A more detailed discussion on this topic is presented in Chapter 3.

### 2.3 The Integration

The integration in equation (2-3) can be separated into two parts:

$$f(\theta_1, \phi_1) = f^{(1)}(\theta_1, \phi_1) + f^{(2)}(\theta_1, \phi_1)$$

$f^{(1)}(\theta_1, \phi_1)$  and  $f^{(2)}(\theta_1, \phi_1)$  denote the intensity distributions of the first ring, and the

second ring respectively.  $f^{(2)}(\theta_1, \phi_1)$  can be found from  $f^{(1)}(\theta_1, \phi_1)$ :

$$f^{(2)}(\theta_1, \phi_1) = f^{(1)}(\theta_2)$$

with  $\theta_2$  the viewing angle with respect to the second (south magnetic pole) axis.  $f^{(2)}$  depends on  $\phi_1$  through the dependence of  $\theta_2$  on  $\theta_1$  and  $\phi_1$ :

$$\cos \theta_2 = -\cos \theta_1 \cos \theta_0 + \sin \theta_1 \sin \theta_0 \cos \phi_1 \quad (2-6)$$

So, we only need to integrate for the first ring:  $f^{(1)}(\theta_1, \phi_1)$ , then  $f^{(2)}$  can be found through it.

The integration is complicated by the fact that the neutron star surface eclipses parts of the ring, and how much of the ring is visible to the observer depends on the orientation of the ring with respect to the line-of-sight. Five cases must be considered:

Case I:  $\theta_1 < \frac{\pi}{2} - \beta_1$  the entire ring is visible.

$$f^{(1)}(\theta_1, \phi_1) = \int_0^{2\pi} \int_{\alpha_1}^{\beta_1} I(\theta') \cos \theta' \sin \theta'' d\theta'' d\phi'' \quad (2-7)$$

Case II:  $\frac{\pi}{2} - \beta_1 < \theta_1 < \frac{\pi}{2} - \alpha_1$  the inner boundary of the ring is entire visible.

$$\begin{aligned} f^{(1)}(\theta_1, \phi_1) = & \int_0^{2\pi} \int_{\alpha_1}^{\left(\frac{\pi}{2} - \theta_1\right)} I(\theta') \cos \theta' \sin \theta'' d\theta'' d\phi'' \\ & + 2 \int_{\left(\frac{\pi}{2} - \theta_1\right)}^{\beta_1} \int_{\phi_1}^{(\arccos[-\cot \theta_1 \cot \theta''] + \phi_1)} I(\theta') \cos \theta' \sin \theta'' d\theta'' d\phi'' \end{aligned} \quad (2-8)$$

Case III:  $\frac{\pi}{2} - \alpha_1 < \theta_1 < \frac{\pi}{2} + \alpha_1$  both the inner and outer boundary are partly eclipsed:

$$f^{(1)}(\theta_1, \phi_1) = 2 \int_{\alpha_1}^{\beta_1} \int_{\phi_1}^{(\arccos[-\cot\theta_1 \cot\theta''] + \phi_1)} I(\theta') \cos\theta' \sin\theta'' d\theta'' d\phi'' \quad (2-9)$$

Case IV:  $\frac{\pi}{2} + \alpha_1 < \theta_1 < \frac{\pi}{2} + \beta_1$  the inner boundary entirely eclipsed but the outer only partly eclipsed:

$$f^{(1)}(\theta_1, \phi_1) = 2 \int_{\left(\theta_1 - \frac{\pi}{2}\right)}^{\beta_1} \int_{\phi_1}^{(\arccos[-\cot\theta_1 \cot\theta''] + \phi_1)} I(\theta') \cos\theta' \sin\theta'' d\theta'' d\phi'' \quad (2-10)$$

Case V:  $\theta_1 > \frac{\pi}{2} + \beta_1$  the entire ring is invisible:

$$f^{(1)}(\theta_1, \phi_1) = 0$$

The derivation of the expressions for the five cases is from Leahy (1991)<sup>[2]</sup> paper. From these equations, we can see two kinds of integrations must be done:

$$F_1(\theta_1, \alpha, \beta) = \int_{\alpha}^{\beta} d\theta'' \int_0^{2\pi} I(\theta') \cos\theta' \sin\theta'' d\phi'' \quad (2-11)$$

$$F_2(\theta_1, \alpha, \beta) = 2 \int_{\alpha}^{\beta} d\theta'' \int_{\phi_1}^{(\arccos[-\cot\theta_1 \cot\theta''] + \phi_1)} I(\theta') \cos\theta' \sin\theta'' d\phi'' \quad (2-12)$$

Then, the five cases can be written as:

$$\text{Case I: } f^{(1)}(\theta_1, \phi_1) = F_1(\theta_1, \alpha_1, \beta_1) \quad (2-13)$$

$$\text{Case II: } f^{(1)}(\theta_1, \phi_1) = F_1\left(\theta_1, \alpha_1, \frac{\pi}{2} - \theta_1\right) + F_2\left(\theta_1, \frac{\pi}{2} - \theta_1, \beta_1\right) \quad (2-14)$$

$$\text{Case III: } f^{(1)}(\theta_1, \phi_1) = F_2(\theta_1, \alpha_1, \beta_1) \quad (2-15)$$

$$\text{Case IV: } f^{(1)}(\theta_1, \phi_1) = F_2\left(\theta_1, \theta_1 - \frac{\pi}{2}, \beta_1\right) \quad (2-16)$$

$$\text{Case V: } f^{(1)}(\theta_1, \phi_1) = 0$$

#### 2.4 Model Fits to the Observed X-ray Pulse Profiles

Observed pulse profiles for 20 binary X-ray pulsars were taken from the literature. Usually the pulse profile for the highest energy range available was chosen, to avoid as much as possible any effects of local photoelectric absorption in the X-ray binary system.

The integration of equation(2-3) gives the intensity as function of  $\theta_1, \theta_2, \phi_1, \alpha_1, \alpha_2, \beta_1, \beta_2$ :

$$f = f(\theta_1, \theta_2, \phi_1, \alpha_1, \alpha_2, \beta_1, \beta_2)$$

In order to get the intensity as function of the pulse phase  $\Phi$ , ( $\Phi = 2\pi t/p + \Phi_0$ ,  $p$  is the period of neutron star rotating), we need the following auxiliary equations which relate  $\theta_1, \theta_2$ , and  $\phi_1$  to  $\Phi$ :

$$\cos\theta_1 = \cos\theta_m \cos\theta_r + \sin\theta_m \sin\theta_r \cos\Phi \quad (2-17)$$

$$\phi_1 - \phi_{ro} = \arccos\left(\frac{\cos\theta_r - \cos\theta_1 \cos\theta_m}{\sin\theta_m \sin\theta_1}\right) \quad (2-18)$$

$$\cos\theta_2 = -\cos\theta_1 \cos\theta_0 + \sin\theta_1 \sin\theta_0 \cos\phi_1 \quad (2-19)$$

with  $\theta_m$  the angle between rotation axis and magnetic axis;  $\theta_r$  the angle between rotation axis and line-of-sight.  $\phi_{r0}$  is the initial azimuthal coordinate of axis Z in  $x'y'z'$  system. Fig 2-5 illustrates these definitions and the relation between the observer's direction and  $z'$  axis of the neutron star.

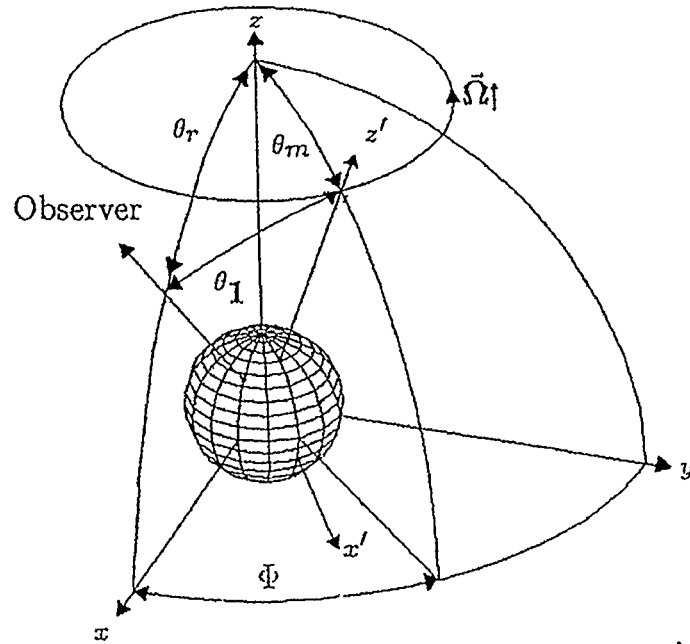


*Fig 2-5* The relation between the observer direction and the neutron star  $z'$  axis showing definitions of associated angles. (Adopted from Leahy 1991)<sup>[2]</sup>.

Then we can have:

$$f = f \left( \underline{\theta}_0, \underline{\theta}_m, \underline{\theta}_r, \underline{\phi}_{r0}, \underline{\alpha}_1, \underline{\alpha}_2, \underline{\beta}_1, \underline{\beta}_2, \underline{\Phi}_0, \underline{\Phi} \right) \quad (2-20)$$

In equation(2-20), the underlined variables are the free parameters needed to be

fitted out for the model. So, there are 10 free parameters altogether for the most general model, including normalization.

The method of least-squares is used in the fitting program. The fitting was done in 8 stages in order to achieve a stable convergence. This is because of the large number of parameters and the model has non-linear dependence on most of the parameters. Specific simpler models were defined by restricting certain parameters. For example, setting the offset angle  $\theta_0$  to zero gave an axially symmetric emitting neutron star; setting  $\alpha$  to zero resulted in a filled polar cap rather than an emission ring. Table 2-1 shows the definition of model types and their parameter numbers.

**Table 2-1 Models and their parameter numbers**

Label	Model	parameter No.
a	Two identical polar caps	5
b	Two identical polar rings	6
c	Two different size polar caps	6
d	Two identical polar caps with offset	7
e	Two identical polar rings with offset	8
f	Two different polar rings	8
g	Two different polar caps with offset	8
h	Two different polar rings with offset	10

## 2.5 The Fitting Program

IMSL routine DUNLSF (Double precision) is used to do the nonlinear least

squares fitting. DUNLSF uses a modified Levenberg-Marquardt method to solve nonlinear least squares problems.

When the light bending is not considered in the model, ( $\theta' = \theta_0'$  in Fig 2-4), equation (2-5) will not be included in the integration (2-3). In this case, the integration will give analytical solutions of  $f(\theta_1, \phi_1)$  for both the  $\cos^2\theta$  and  $\cos^4\theta$  models, which are stated in the paper of Leahy (1991)<sup>[2]</sup>. However, when the effect of light bending is considered, and equation (2-5) is included in the integration, no analytical solutions can be obtained for  $f(\theta_1, \phi_1)$ . Numerical integrations have to be used in the fitting program, which will make the program complicated and slow, and much more difficult to achieve stable convergence.

The light bending equation (2-5) is also a complicated integration from which no analytical form can be obtained. Straightening out this equation by finding a simple analytical fitting for it can greatly simplify the integration for  $f(\theta_1, \phi_1)$ , thus greatly speed up the fitting program. Please see the Appendix for more details of the program. Chapter 3 will deal with the light bending problem.

## CHAPTER 3

### GRAVITATIONAL LIGHT BENDING

#### 3.1 Introduction

Deflection of light in a gravitational field is presently one of the three experimentally measurable consequences of general relativity. The other two are: (1) the red shift; (2) the perihelion precession of Mercury. Modifications to the gravitational field strength due to general relativity become important when considering the properties of compact objects like neutron stars. Indeed, it is largely for this reason that compact objects are of such great theoretical interest.

If the original mass of the progenitor star is greater than about eight to ten solar masses, the direct collapse of the stellar core can possibly produce a neutron star. The collapse of the core in the supernova can be halted only when the degeneracy pressure of the particles in the core has grown to the point where it can balance gravity. In neutron stars, it is the neutrons that are degenerate and provide the necessary opposition to the gravity forces (Landau 1932<sup>[10]</sup>; Baade & Zwicky 1934 a<sup>[11]</sup>, b<sup>[12]</sup>; Oppenheimer and Volkoff, 1939<sup>[13]</sup>). Based on this theory, the mass and radius of neutron star can be estimated from the models of the equation of state.

For the current models (Shapiro and Teukolsky 1983)<sup>[14]</sup>, the radius of neutron star,  $r_0$ , are approximately in the range:  $2 \leq r_0 \leq 4$ , where  $r_0$  is in the unit of Schwarzschild radius  $R_s$  ( $R_s = 2GM/c^2$ ). In this case, gravitational light bending is expected to occur near the neutron star surface. Riffert & Mészáros (1988)<sup>[9]</sup> give an expression for general relativity light bending in the form of a complicated integration (equation 2-5). In this chapter, we will find a linear

fitting for this equation, which will greatly simplify the model.

### 3.2 The Light Bending Equation

In special relativity, the motion of a particle that is not acted on by any forces is represented by a straight line in Minkowski space-time. In general relativity, using Riemannian space time, the motion is represented by a line that is no longer straight (in the Euclidean sense) but is the line giving the shortest distance. Such a line is said to be curved. In the theory of general relativity, gravitational effects may be explained by the curvature of space-time.

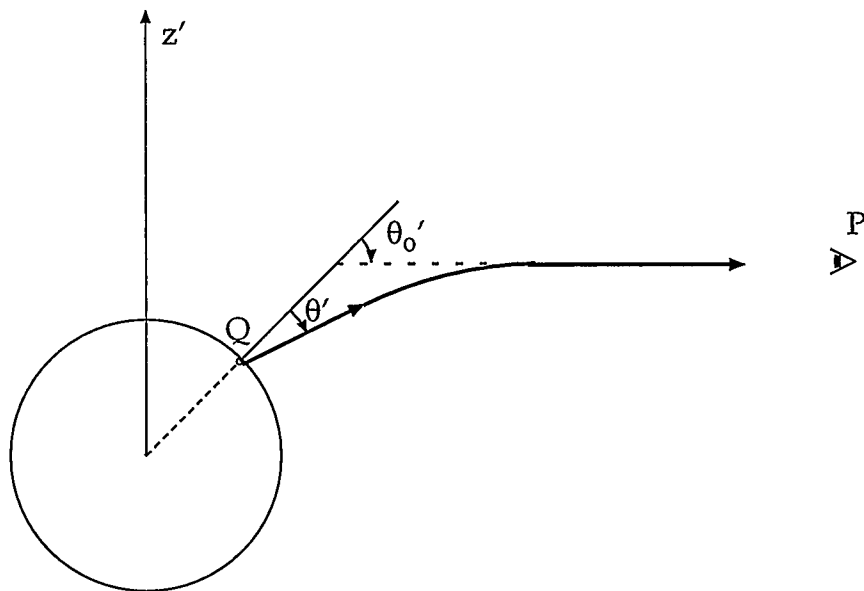


*Fig 3-1* Geometry of the light bending, showing coordinates of emission point  $Q$  ( $r_0, \theta'', \phi''$ ) and the observer point  $P$  ( $r, \theta_1, \phi_1$ ). ( $r \rightarrow \infty$ ). (Compare with Fig 2-4).

Fig 3-1 shows the geometry of the light bending near the surface of a neutron star. The thick black line indicates the path of the light. We usually take the

observer P at infinity ( $r \rightarrow \infty$ ).

To obtain the orbit of photons (and any other particles having rest mass equal to zero) in the gravitational field, we may use the Geodesics equation (the differential equation of the curve having an extreme length:  $\delta I = \delta \int L ds = 0$ ) along with the condition  $ds = 0$ , namely, the null geodesics. (See Misner, Thorne, and Wheeler 1973)<sup>[15]</sup>. From the orbit equations, the relation between  $\theta'$  and  $\theta_0'$  can be found:

$$\theta_0'(r, r_0, \mu) = b \int_{r_0}^r \frac{1}{x} \left[ x^2 - b^2 \left( 1 - \frac{1}{x} \right) \right]^{-1/2} dx \quad (2-5)$$

Where:

$$\mu = \cos \theta'$$

$$b = \frac{r_0}{A_0} (1 - \mu^2)^{1/2}; \text{ relativistic impact parameter}$$

$$A_0 = \left( 1 - \frac{1}{r_0} \right)^{1/2}$$

$$r_0 = \frac{Rc^2}{2GM} \quad (\text{Neutron star radius in Schwarzschild units})$$

The integration of equation (2-5) has no analytical solution. In order to make the incorporation of this equation into the modelling program practically possible, we need to fit out a simple form for equation (2-5).

### 3.3 The Linear Fittings to the Light Bending Equation

Very simple linear relations between  $\cos \theta_0'$  and  $\cos \theta'$  can be fitted out from the

numerical calculations of equation (2-5). For  $r_0 \geq 2$ , these straight line fittings are perfect, and the bigger the  $r_0$ , the better the fitting. (See Fig 3-2 for two examples). However, when  $r_0 < 2$ , the plots of  $\cos\theta_0'$  vs.  $\cos\theta'$  are obviously curved, linear fittings are not very suitable in these cases (see Fig 3-4).

Fig 3-2 shows the fittings for two typical values of neutron star radius: a)  $r_0=2.4184$ , the estimated radius for most neutron stars, whose  $R=10$  km,  $M=1.4$  solar mass; b)  $r_0=4.4008$ , the estimated radius for Her X-1, whose  $R=13$  km,  $M=1.0$  solar mass (see Mészáros 1992<sup>[16]</sup>).

If we use  $a$  and  $b$  to denote the slope and intercept of the fitted straight line respectively, we can see that  $a$  and the absolute value of  $b$  become smaller when  $r_0$  increases (see Table 3-1).  $r_0$  implies the density of the star, the bigger  $r_0$  corresponds to smaller density;  $a$  and  $|b|$  are indications of the gravitational effects, smaller  $a$  and  $|b|$  mean less gravitational effects in comparison. When  $r_0$  increases, the decrease of the star density will result in smaller modification to general relativity, thus  $a$  and  $|b|$  will decrease. So strong correlations exist between  $a$  —  $r_0$  and  $b$  —  $r_0$ . For  $r_0$  in the reasonable range for neutron star:  $2 \leq r_0 \leq 5$ , these correlations can also be perfectly fitted out using very simple formulae (see Fig 3-3). When  $r_0 > 5$ ,  $a$  and  $b$  will deviate from the fitted curve of Fig 3-3 (a) and Fig 3-3 (b). Thus, these fittings should be performed separately in different ranges, i.e., the neutron star range, the white dwarf range and the normal star range, etc. In this thesis, only the neutron star is of concern, thus the fittings for  $r_0$  in the range  $[2,5]$  will be used.

Table 3-1 lists the slope ( $a$ ) and intercept ( $b$ ) of the fitted straight lines for

different  $r_0$ :

**Table 3-1 Fitted slope (a) and intercept (b) for different  $r_0$**

$r_0$	a	b	$r_0$	a	b	$r_0$	a	b
2.0	1.922	-0.942	3.0	1.490	-0.493	4.0	1.330	-0.330
2.2	1.789	-0.800	3.2	1.446	-0.448	4.4008	1.291	-0.292
2.3	1.734	-0.743	3.3	1.427	-0.429	4.6	1.275	-0.276
2.4184	1.678	-0.684	3.4	1.410	-0.411	5.0	1.248	-0.248
2.5	1.642	-0.648	3.5	1.394	-0.395	50.0	1.020	-0.020
2.6	1.604	-0.609	3.6	1.379	-0.380	100	1.010	-0.100
2.8	1.542	-0.545	3.8	1.352	-0.354			

Thus, the light bending equation (2-5) can be replaced by the following simple equations:

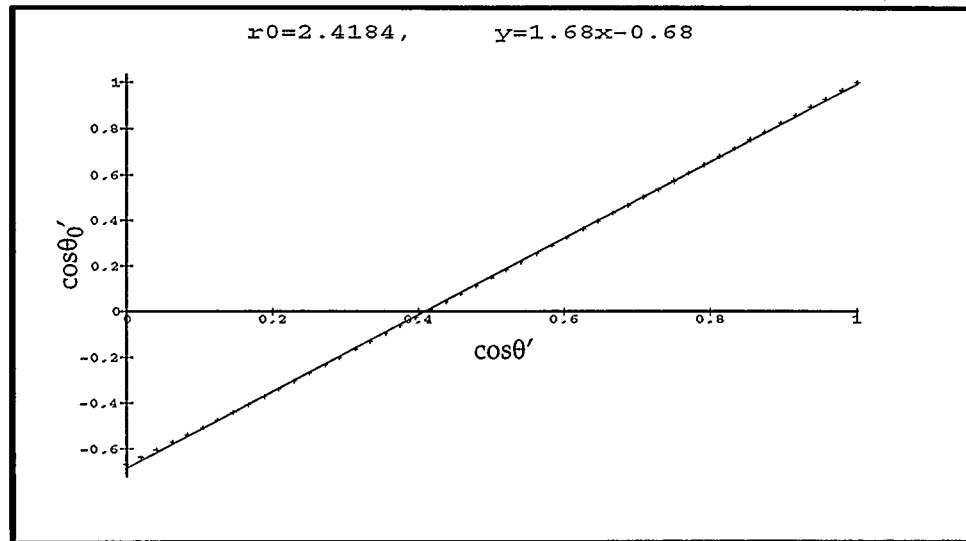
$$\cos\theta_0' = a \cdot \cos\theta' + b \quad (3-1)$$

Where:

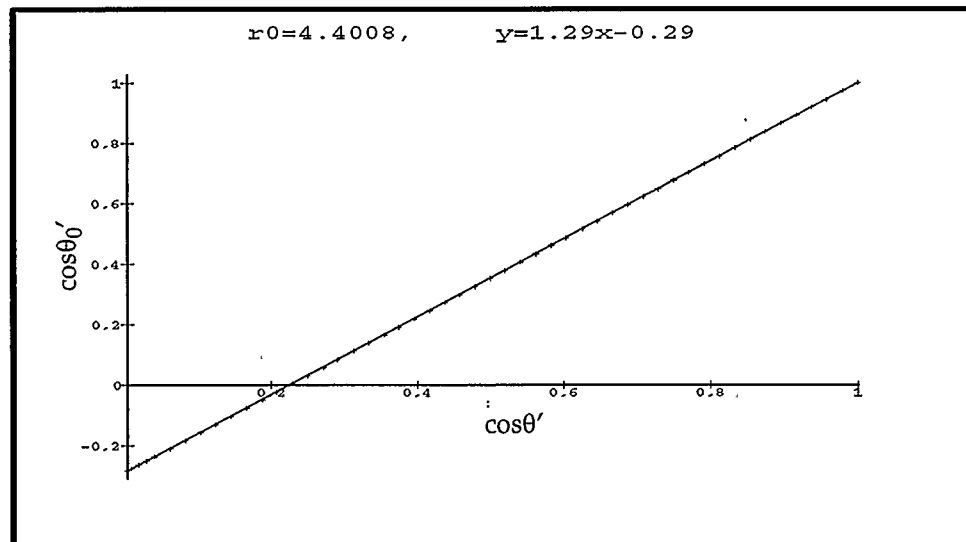
$$a = \frac{2.653}{r_0^2} + \frac{0.381}{r_0} + 1.068 \quad (3-2)$$

$$b = -\frac{2.944}{r_0^2} - \frac{0.232}{r_0} - 0.087 \quad (3-3)$$

$$(2 \leq r_0 \leq 5)$$

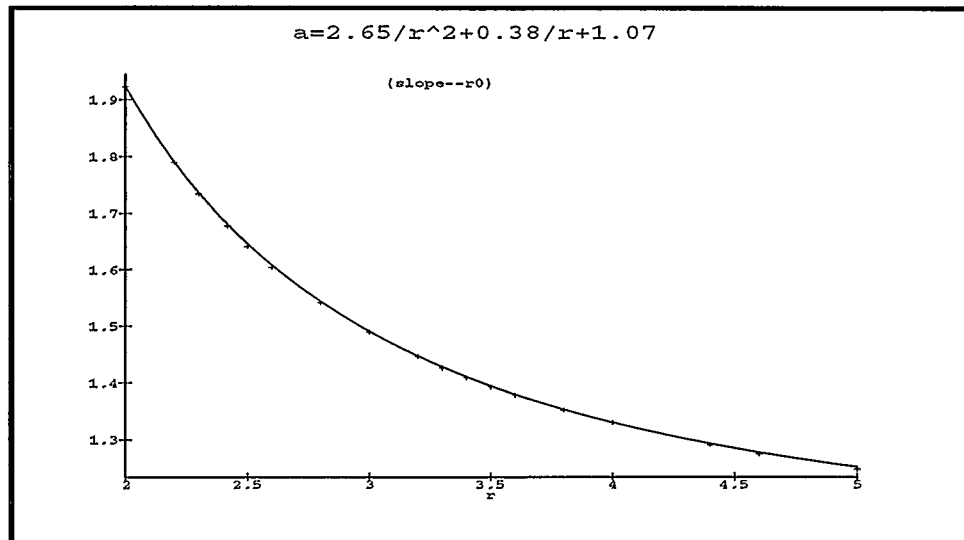


(a)

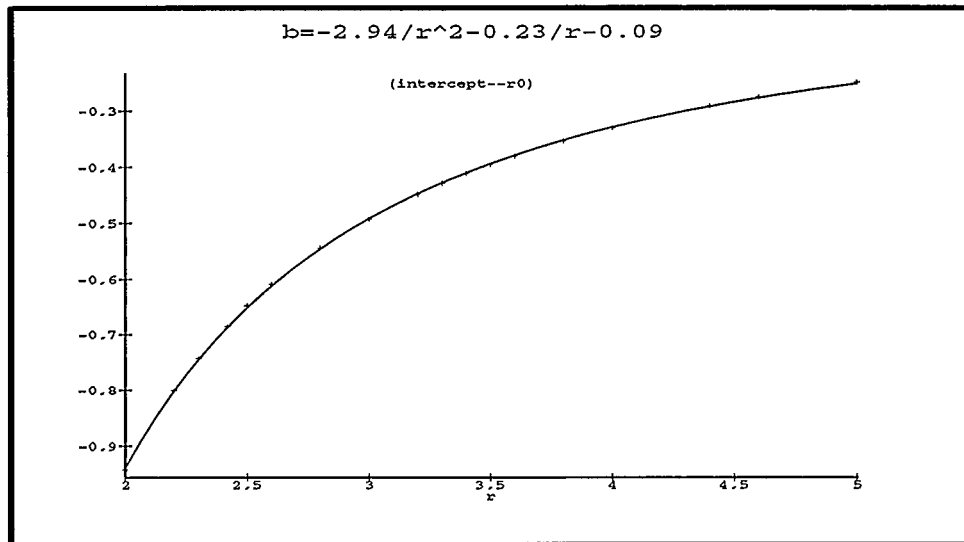


(b)

*Fig 3-2* Linear fittings of the light bending formula (equation 2-5) for two typical values of neutron star radius: a)  $r_0 = 2.4184$ , for most neutron stars; b)  $r_0 = 4.4008$ , for Her X-1. The data points are numerical calculations from equation (2-5).



(a)



(b)

Fig 3-3 a) Fitted relation between slope and  $r_0$  ( $2 \leq r_0 \leq 5$ ).

b) Fitted relation between intercept and  $r_0$  ( $2 \leq r_0 \leq 5$ ).

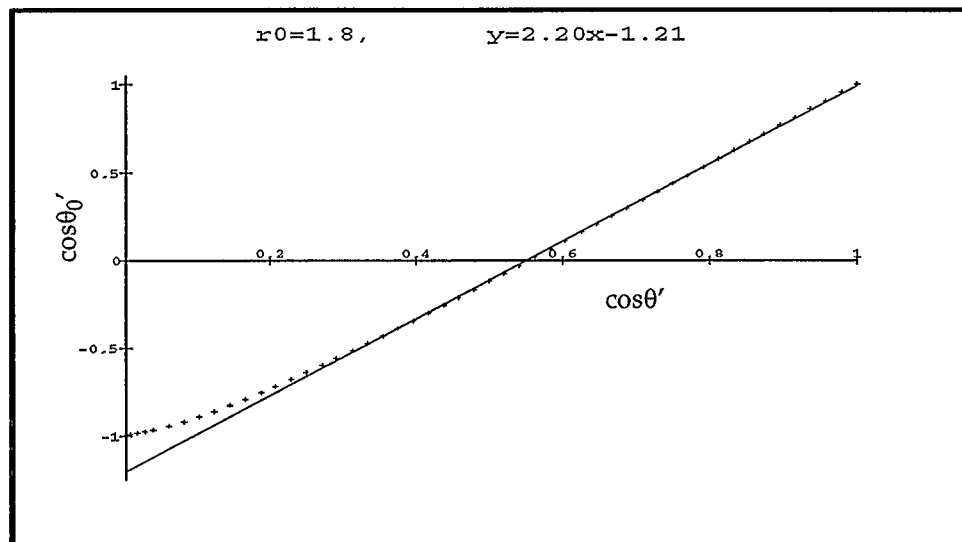
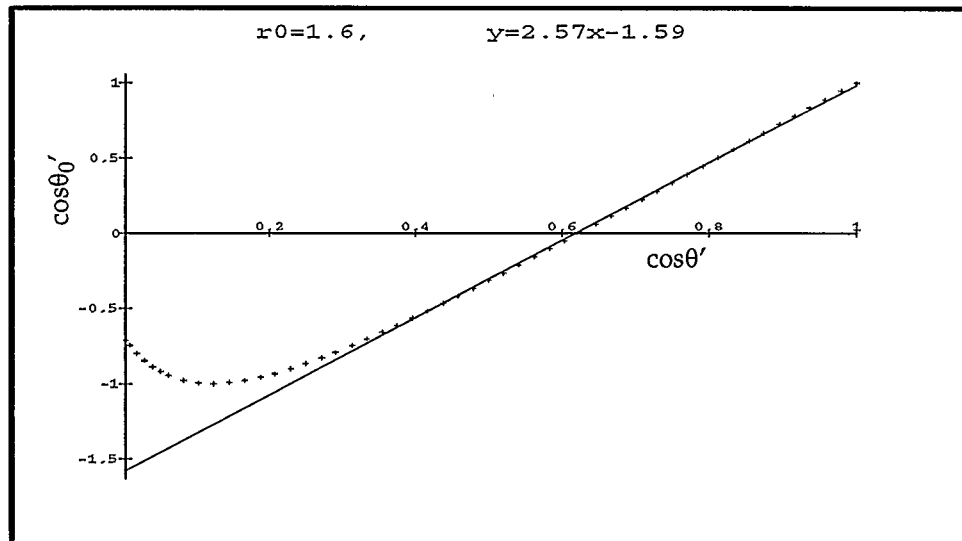


*Fig 3-4* When  $r_0 < 2$ , the plot of  $\cos\theta_0'$  vs.  $\cos\theta$  is obviously curved, the data points deviate from a straight line. Linear fitting is not suitable for the full range of  $\cos\theta'$ , but still perfect in a smaller range:  $[0.4, 1]$  for  $r_0=1.6$ ;  $[0.3, 1]$  for  $r_0=1.8$ . (The data points are numerical calculations from equation 2-5).

## CHAPTER 4

### Fitting of the Pulsar Profile: The Effects of Relativistic Light-Bending

#### 4.1 Introduction

In the emission model, the size of the emission area is determined by the interaction of the distant accretion flow with the stellar magnetosphere. An order-of magnitude estimate can be obtained by calculating the last closed magnetic line within the Alfvén radius where the ram pressure of the accretion flow is balanced by the magnetic pressure. This usually leads to a rather small emission region; in particular, for the case of a thin accretion disk in a dipole magnetic field, (Riffert. et al. 1993)<sup>[17]</sup>,

$$\sin\beta = 0.189\alpha^{1/61}\dot{m}^{8/61}m^{-9/61}R^{-59/61}B_{12}^{-20/61} \quad (4-1)$$

where  $B_{12}$  is the magnetic field around the neutron star in units of  $10^{12}$  G,  $\dot{m}$  is the accretion rate in Eddington units,  $m$  is the mass in solar units,  $R$  is the stellar radius in units of the Schwarzschild radius, and  $\alpha$  denotes the disk viscosity parameter. For magnetic fields  $B_{12} \approx 1$ , a radius  $R \approx 2$ , and other parameters of order unity, a polar cap angle  $\beta$  of  $5^\circ$ — $10^\circ$  is obtained.

In this chapter, the light bending effect will be included in the fitting program. The results are compared to the model without light bending. The light bending model gives a more symmetric and smaller emission region, making it more consistent with the theoretical estimate discussed above.

## 4.2 The Observations of X-ray Pulsars

Since the discovery of the first X-ray pulsar in the Crab Nebula, X-ray astronomy satellites, such as Uhuru, Ariel V, SAS 3, HEAO 1, Einstein, Tenma, EXOSAT, and Ginga, have been used to find new X-ray pulsars, and more than two dozen X-ray pulsars have been confirmed so far.

X-ray pulsars can be classified into three categories (e.g., Blair & Candy 1985<sup>[18]</sup>):

(A) Binaries with early type companions (Cen X-3, Vela X-1, GX 301-2 etc.).

The Pulsars in this class can be divided into two subclasses (Corbet 1986<sup>[19]</sup>, Stella et al. 1986<sup>[20]</sup>):

(A-i) The short pulse-period systems (SMC X-1, Cen X-3, LMC X-4 etc.) with very large X-ray luminosity.

(A-ii) The long pulse-period systems (Vela X-1, GX 301-2, 4U1538-52, 4U 1907+09, etc.) with moderate X-ray luminosity.

(B) Binaries with Be-star companions (4U0115+63, A 0535+26, GX 304-1, X Per etc.)

(C) Low-mass binaries (Her X-1, GX 1+4, 4U1626-67 etc.).

X-ray pulsars in class (A-i) and (C) are mostly powered by mass accretion via Roche-lobe overflow (so-called "disk-fed" pulsars), whereas those in class (A-ii) and (B) are considered to be powered by mass accretion via stellar wind captures (so-called "wind-fed" pulsars). The observed pulse profiles can be classified into several patterns (Nagase, 1989<sup>[21]</sup>):

- (a) Single sinusoidal-like shapes with little dependence on energy (X Per, GX 304-1, etc.).
- (b) Sinusoidal-like double peaks with little energy dependence (GX 301-2, 4U 1538-52, SMC X-1 etc., the amplitudes of the two peaks are usually different).
- (c) An asymmetric single peak with some features (Cen X-3, GX 1+4 etc.).
- (d) A single sinusoidal-like peak at high and low energies and close adjacent double peaks in the intermediate energy range (Her X-1, 4U 1626-67 etc., the phase of the maximum amplitude at low energies reversed by  $180^\circ$  with respect to that at higher energies for some sources).
- (e) Double sinusoidal-like peaks at high energies and complex five peaks at low energies (Vela X-1, A 0535+26 etc.).

Table 4-1 lists some observed properties with the references of the 7 pulsars which will be studied in this thesis, in the order of increasing pulse period:

**Table 4-1 X-ray Pulsars**

Source	Pulse period (s)	Energy range (keV)	X-ray luminosity ( $\times 10^{36}$ erg $s^{-1}$ )	Ref
4U0115+63	3.61	0.9 - 13.3	10	[22]
Cen X-3	4.84	12.5 - 25	79	[23]
4U1626-67	7.68	14 - 30	13	[23]
4U1258-62	272	7 - 25	0.6	[23]

**Table 4-1 X-ray Pulsars**

Source	Pulse period (s)	Energy range (keV)	X-ray luminosity ( $\times 10^{36}$ erg $s^{-1}$ )	Ref
4U0900-40	283	25 - 60	2.5	[23]
4U1118-61	405	1.5 - 15	5	[22]
GPS1722-36	413	9 - 19	not known	[21]

### 4.3 The Model Fits to the Pulsar Profiles

Differences in X-ray pulse profiles are considered to be due to the differences in the geometrical configuration with respect to the rotational axis  $Z$  of the neutron star, the axis of the magnetic dipole moment  $Z'$ , and the observer's line of sight (see Fig 2-4 on page 8 and Fig 2-5 on page 14). The Model described in Chapter 2 can be used to figure out the geometry structures of neutron stars.

Table 4-2 lists the fitted parameters from both the no light-bending model and the light-bending model. Both the two analytical functions for the intensity distribution were used for the model:  $I(\theta') \cos\theta' = A \cos^2\theta'$ ; and  $I(\theta') \cos\theta' = A \cos^4\theta'$ . Generally, the  $\cos^2\theta'$  model will give better fittings, especially when the light-bending effect is included. The fittings listed in the table are all  $\cos^2\theta'$  model, except 4U1626-67, for which the  $\cos^4\theta'$  model gives a much better fitting. For each object in the table, the first row lists the parameters for the no light-bending model, while the second row lists the parameters for the light-bending model. The goodness of fit was not performed for the fittings, because the statistical errors were not available for the majority of the published pulse profiles. However, restricted to a given pulsar, the resulting least sum-of-squares (SSQ) gives a relative measure of goodness of fit for comparing the

different models (e.g., the  $\cos^2\theta'$  model and the  $\cos^4\theta'$  model; the no light-bending model and the light-bending model, etc.).

**Table 4-2 Pulse profile model parameters**

Pulsar <sup>a</sup>	Rotational & magnetic axis angles <sup>b</sup> : $\theta_m, \theta_r$	Emission ring angles <sup>b</sup> $\alpha_1, \beta_1, \alpha_2, \beta_2$	Offset angle <sup>b</sup> : $\theta_o$
4U0115+63 <sup>c</sup>	1.515, 0.530	0.599, 0.622, 0.561, 0.583	0.595
	1.632, 0.499	0.602, 0.618, 0.562, 0.581	0.007
Cen X-3 <sup>c</sup>	1.461, 0.368	0.287, 0.433, 0.558, 0.602	0.759
	1.541, 0.415	0.238, 0.444, 0.555, 0.616	0.020
4U1626-67 <sup>d</sup>	0.246, 0.246	0.000E0, 0.068, 0.200, 0.300	0.100
	0.320, 0.321	0.129E-4, 0.034, 0.200, 0.300	0.100
4U1258-62 <sup>c</sup>	1.252, 0.168	0.465, 0.487, 0.405, 0.428	0.507
	1.212, 0.118	0.472, 0.482, 0.400, 0.430	0.218
4U0900-40 <sup>c</sup>	1.427, 0.617	0.468, 0.501, 0.357, 0.482	0.172
	1.407, 0.655	0.411, 0.464, 0.634, 0.292	-0.167
4U1118-61 <sup>c</sup>	0.602, 0.602	0.000E0, 0.035, 0.040, 0.052	0.100
	0.838, 0.823	0.051, 0.060, 0.056, 0.058	-0.415
GPS 1722-36 <sup>c</sup>	0.851, 0.902	0.488, 0.690, 0.565, 0.770	0.437
	0.520, 1.269	0.108, 0.740, 0.672, 0.684	0.674
a. The first row for each object lists parameters for no light-bending model, the second row lists parameters for light-bending model.			
b. The unit for angles is radians.			
c. The intensity distribution used in the models is $\cos^2\theta'$ .			
d. The intensity distribution used in the models is $\cos^4\theta'$ .			

Table 4-3 shows the comparison of the two models: no light-bending model and light-bending model, where the solid angle of the neutron star is given by:

$$\Omega = \int \sin\theta d\theta d\phi \quad (4-2)$$

and the emitting area is:  $A = \Omega R^2$ , with R the radius of the neutron star.

#### 4.4 The Fitted Profiles for X-ray Pulsars

Fig 4-1 — Fig 4-7 show the pulsar profiles. We can see that the light-bending model can give more sharp fittings to the peaks and dips of the profiles. Fig A-3 on page 66 is the overview of the equations. From this figure we can see that, if the light-bending effect is ignored,  $\theta'$  is the same as  $\theta'_0$ , the radiation pattern is:

$$I(\theta') \cos\theta' = B \cos^2\theta' = B \cos^2\theta'_0 \quad (4-3)$$

The integration over this  $\cos^2\theta'_0$  pattern will give relatively flat profiles. The radiation pattern including the effect of light-bending is:

$$I(\theta') \cos\theta' = B \cos^2\theta' = B (c \cos\theta'_0 + d)^2 = e \cos^2\theta'_0 + f \cos\theta'_0 + g \quad (4-4)$$

Where  $c, d, e, f, g$  are constants.

Here, the  $\cos\theta'_0$  and the constant term in the radiation pattern can give sharper features in the profile. That's why the profile of the light-bending model is more flexible and can better fit the observation.

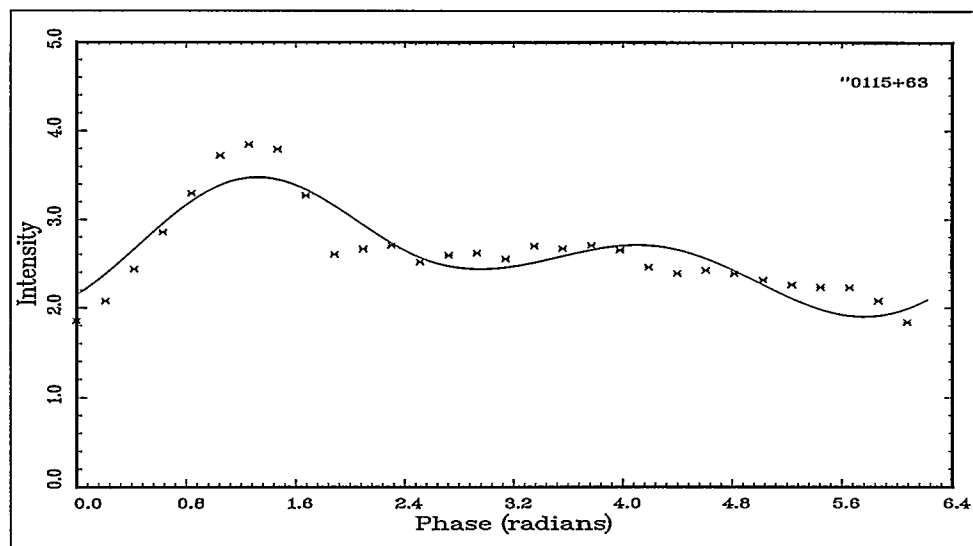
Table 4-3 Comparison of the two models

Pulsar <sup>a</sup>	SSQ <sup>b</sup>	Solid angle of the emission region: $\Omega$	Comments <sup>e</sup>
4U0115+63 <sup>c</sup>	1.499	0.1556	SSQ: ↓ 11.2%; Size: ↓ 22.4%; $\theta_o$ : ↓ 98.8%.
	1.331	0.1208	
Cen X-3 <sup>c</sup>	0.342	0.7299	SSQ: ↓ 52.0%; Size: ↓ 11.7%; $\theta_o$ : ↓ 97.4%.
	0.164	0.6444	
4U1626-67 <sup>d</sup>	0.668	0.1699	SSQ: ↓ 0.6 %; Size: ↓ 6.5%; $\theta_o$ : the same.
	0.664	0.1589	
4U1258-62 <sup>c</sup>	0.029	0.1207	SSQ: ↓ 20.7%; Size: ↓ 13.8%; $\theta_o$ : ↓ 57.0%.
	0.023	0.1041	
4U0900-40 <sup>c</sup>	0.339	0.4149	SSQ: ↓ 76.4%; Size: ↓ 5.4%; $\theta_o$ : ↓ 2.9%.
	0.080	0.3927	
4U1118-61 <sup>c</sup>	0.213	0.0073	SSQ: ↓ 76.8%; Size: ↓ 50.7%; $\theta_o$ : ↑ 315%.
	0.049	0.0036	
GPS 1722-36 <sup>c</sup>	4.249	1.5009	SSQ: ↓ 9.2%; Size: ↑ 11.0%; $\theta_o$ : ↑ 54.2%.
	4.210	1.6655	
a. The first row for each object lists parameters for no light-bending model, the second row lists parameters for light-bending model.			
b. SSQ: Sum of squared deviations			
c. The intensity distribution used in the models is $\cos^2\theta'$ .			
d. The intensity distribution used in the models is $\cos^4\theta'$ .			
e. This column compares the light-bending model with the no light-bending model. Size: the area of the emission region, which equals $\Omega R^2$ , with R the neutron star radius. ↓ : decreased. ↑: increased, on the value of no light-bending model.			

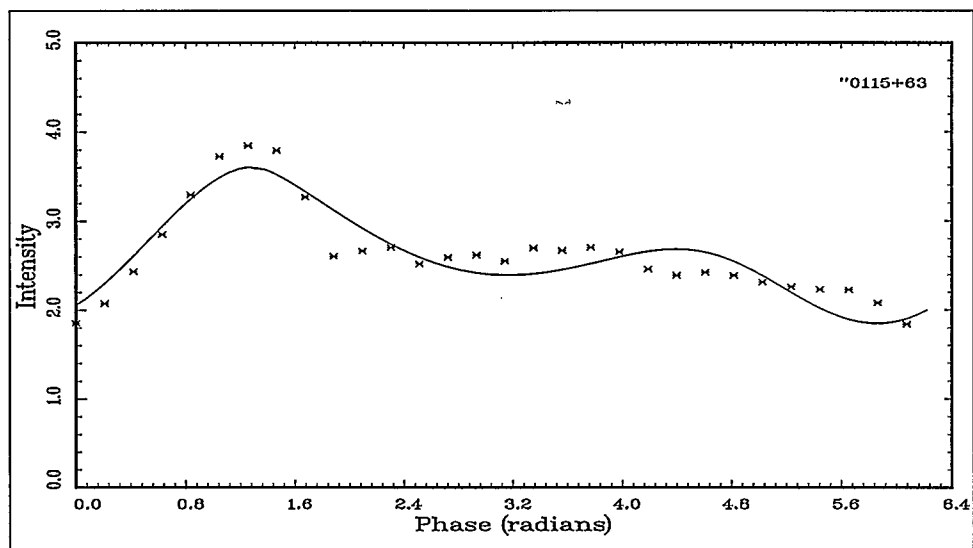
#### 4.5 Conclusion

From Table 4-2 and 4-3 we can see that after the effect of the light bending is included, for all the 7 pulsars, SSQ (sum of squared deviations) decreased. The relative decreases range from 0.6% (4U1626-67) to 76.8% (4U1118-61); 5 of the 7 pulsars get smaller  $\theta_o$ , only 2  $\theta_o$ s increased, the decreases of  $\theta_o$  range from 0% (4U1627-67) to 98.8% (4U0115+63); for 6 pulsars, the area of the emission region decreased, from 5.4% (4U0900-40) to 50.7% (4U1118-61), with only GPS1722-36 as an exception, whose size increased 11.0%.

Generally speaking, with so many parameters, the model fit is not unique. Usually, quite different parameters can be obtained while SSQ is not significantly different. In this case however, though goodness of fit can not be performed, we take SSQ as a relative measurement of goodness of fit, and the model fit with smaller SSQ is the better fit. Then we may conclude that the model including the effects of light-bending gives better fittings to the observations, and geometric pictures more consistent with theoretical estimates.

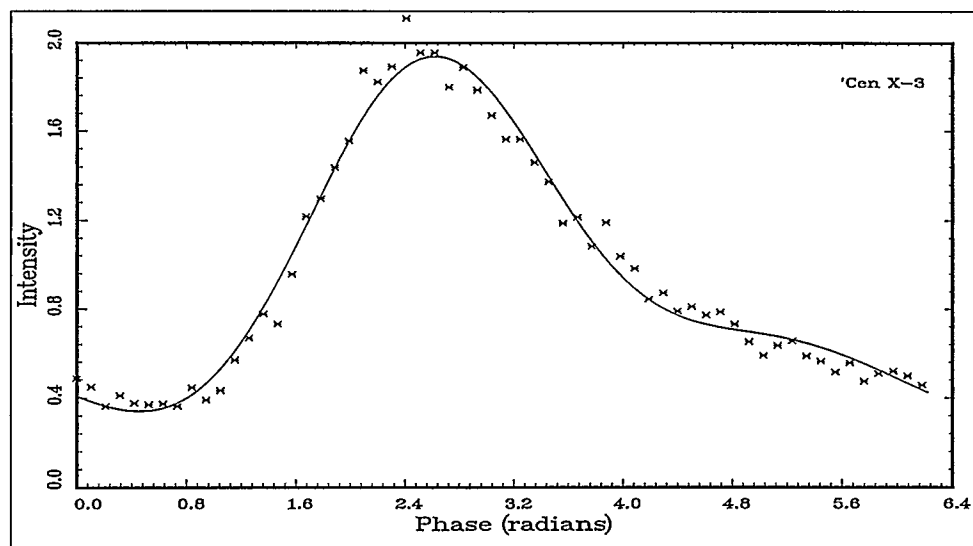


(a)

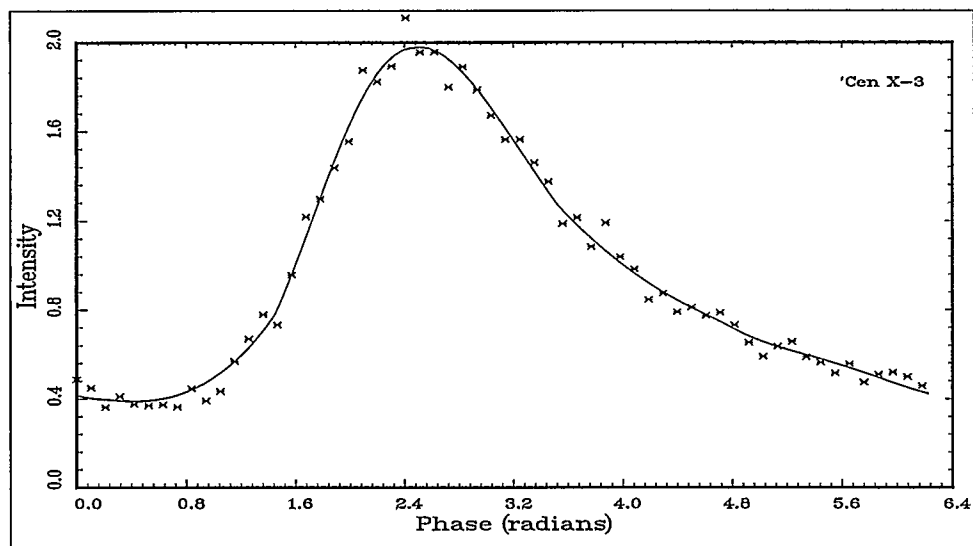


(b)

*Fig 4-1* Pulsar Profiles for 4U0115+63. (a) Profile for no light-bending model,  $SSQ=1.499$ . (b) Profile for light-bending model,  $SSQ=1.331$ .

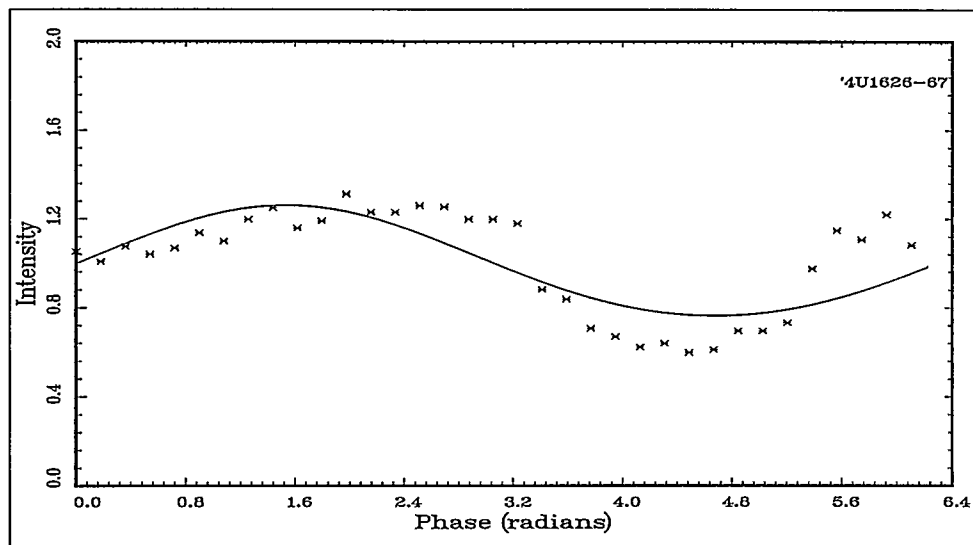


(a)

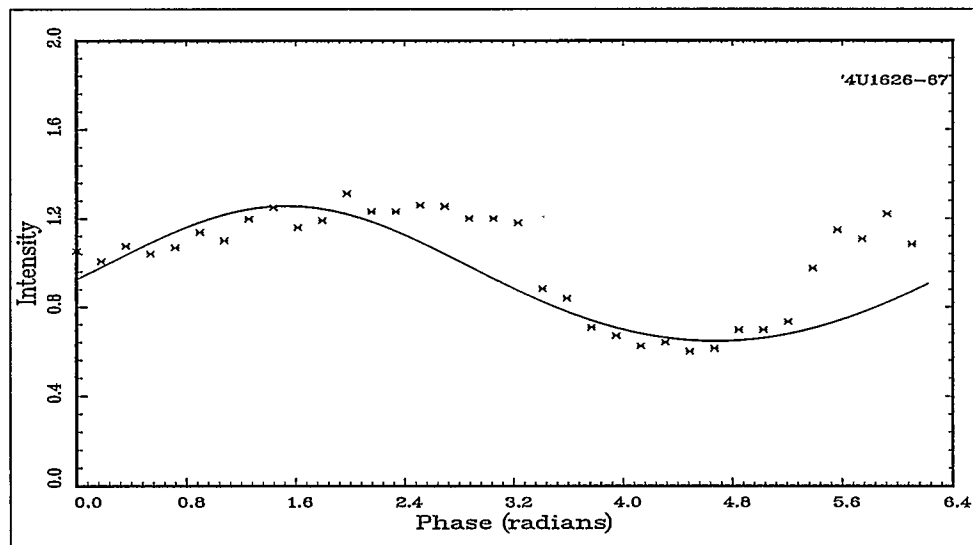


(b)

Fig 4-2 Pulse profiles for Cen X-3. (a) Profile for no light-bending model,  $SSQ=0.342$ . (b) Profile for light-bending model,  $SSQ=0.164$ .

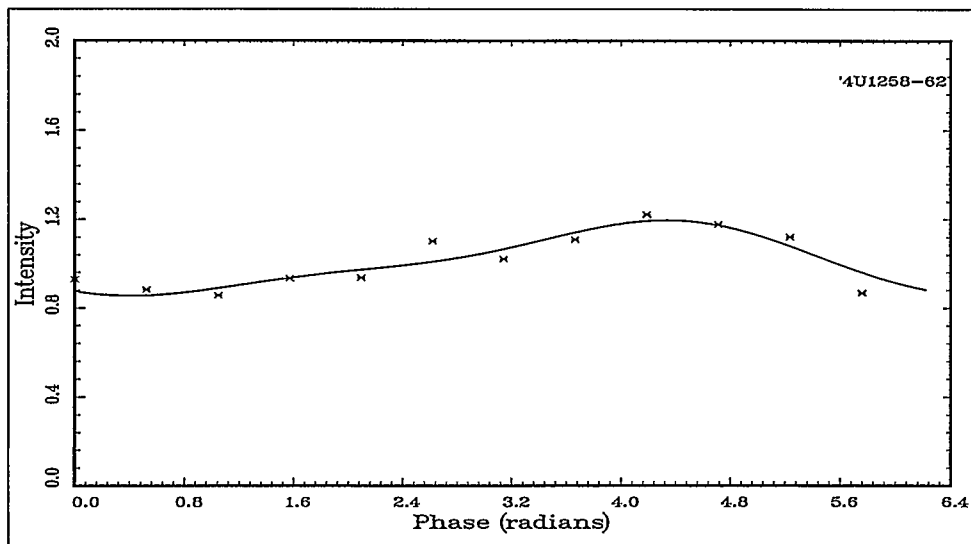


(a)

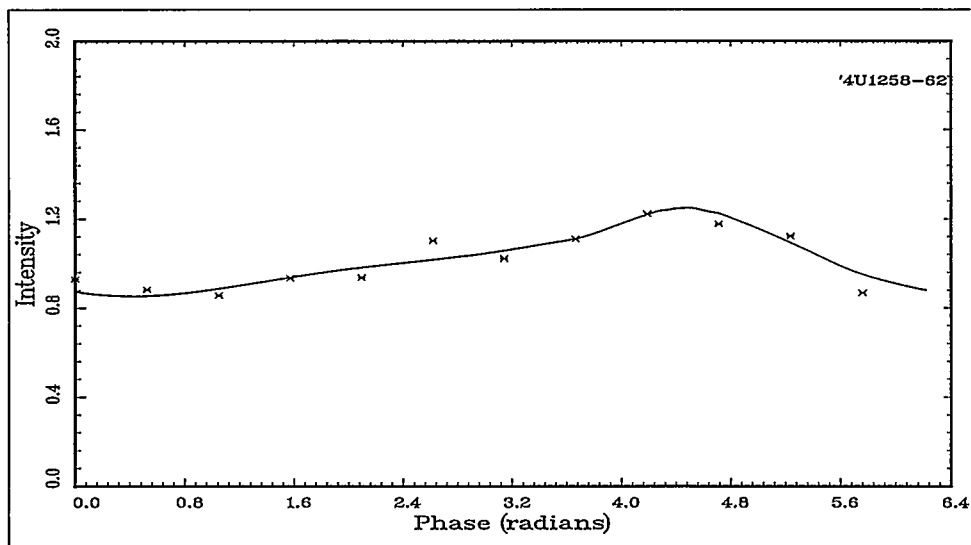


(b)

*Fig 4-3* Pulse profiles for 4U1626-67. (a) Profile for no light-bending model,  $SSQ=0.668$ . (b) Profile for light-bending model,  $SSQ=0.664$ .

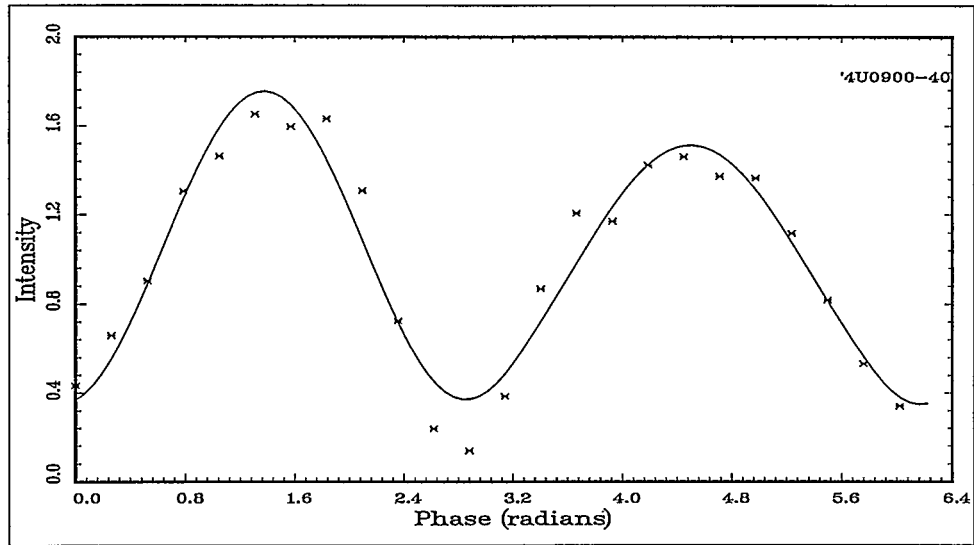


(a)

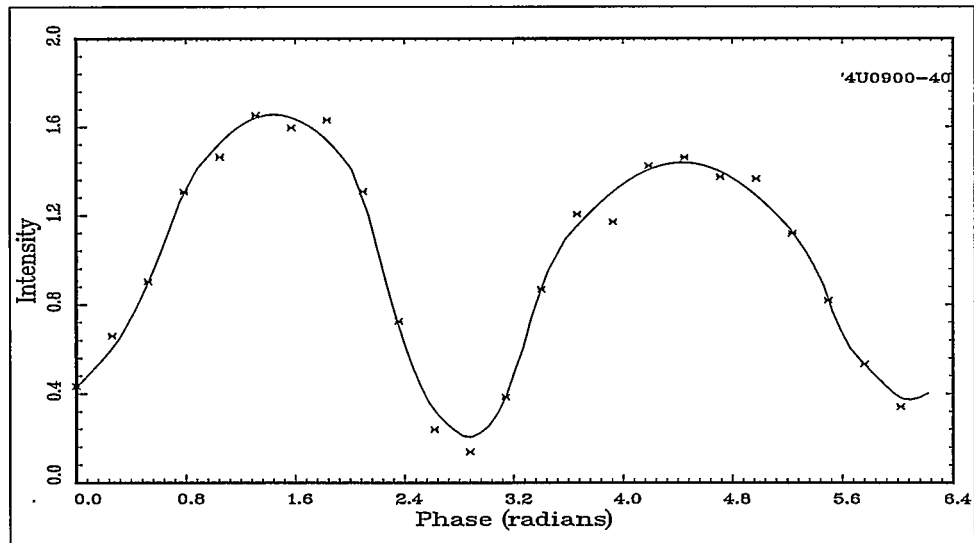


(b)

Fig 4-4 Pulse profiles for 4U1258-62. (a) Profile for no light-bending model,  $SSQ=0.029$ . (b) Profile for light-bending model,  $SSQ=0.023$ .

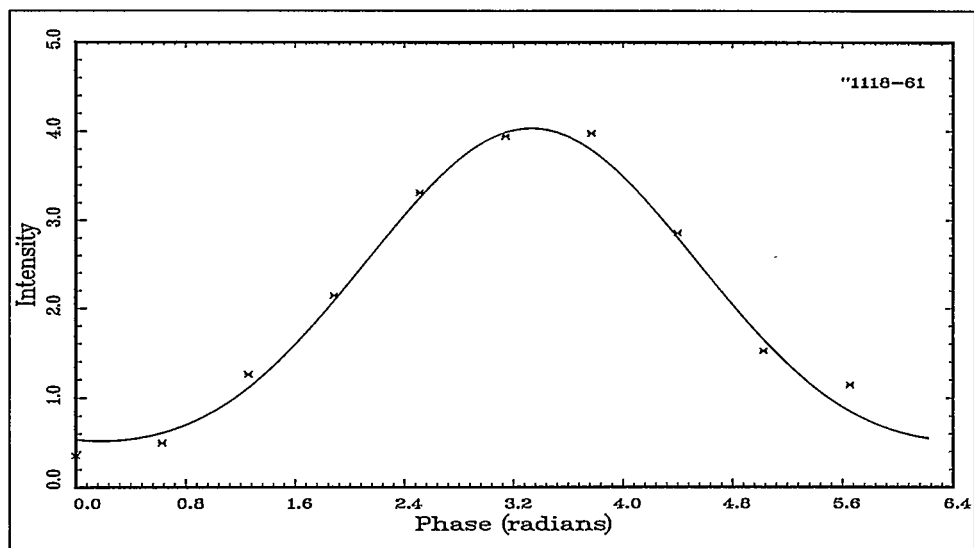


(a)

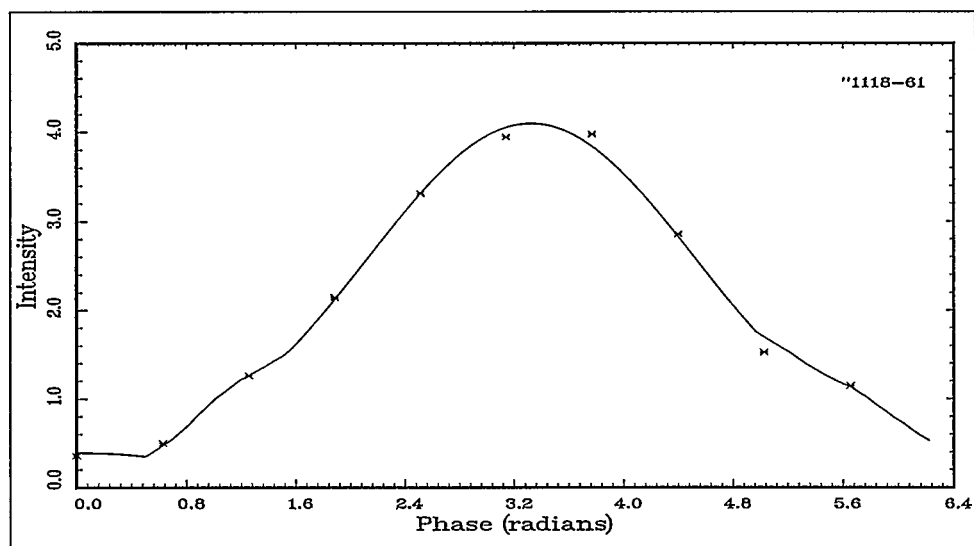


(b)

Fig 4-5 Pulse profiles for 4U0900-40. (a) Profile for no light-bending model,  $SSQ=0.339$ . (b) Profile for light-bending model,  $SSQ=0.080$ .

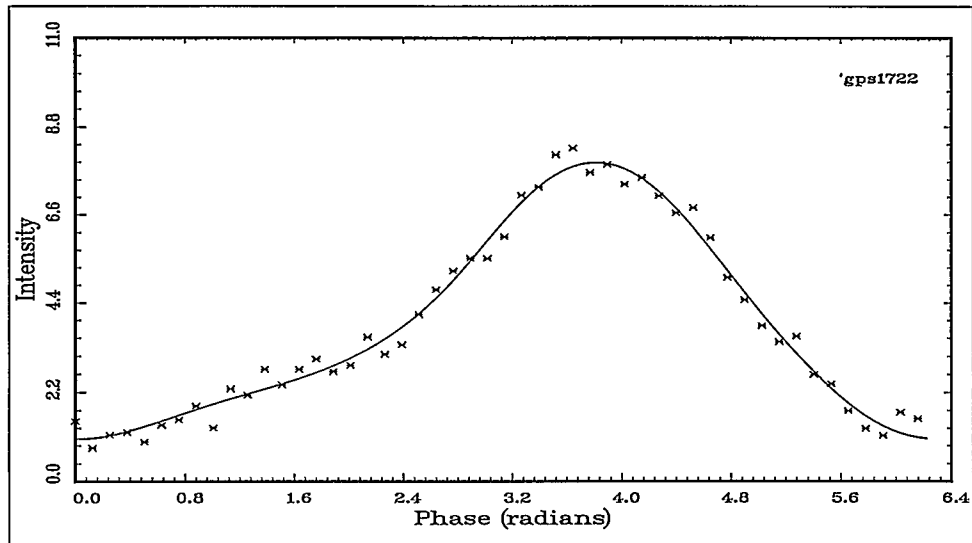


(a)

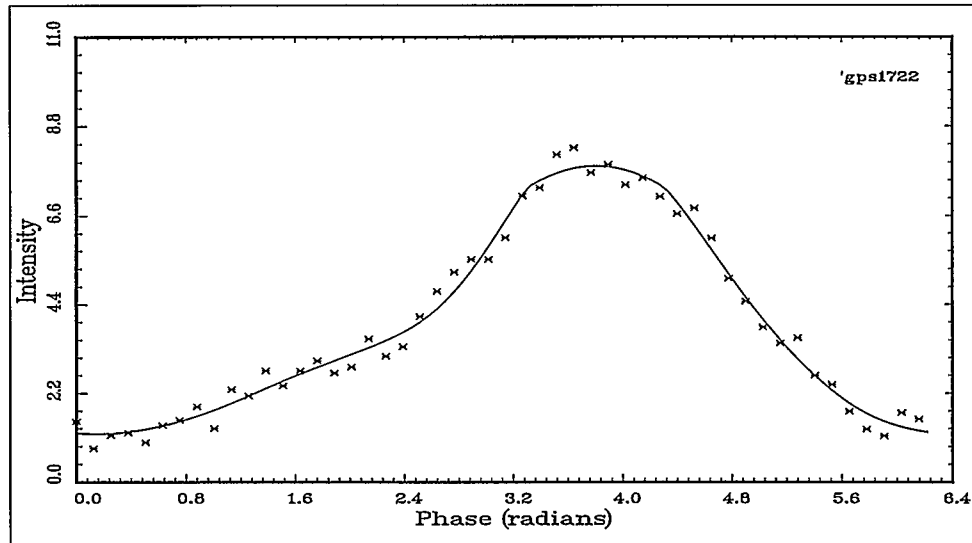


(b)

Fig 4-6 Pulse profiles for 4U1118-61. (a) Profile for no light-bending model,  $SSQ=0.213$ . (b) Profile for light-bending model,  $SSQ=0.049$



(a)



(b)

Fig 4-7 Pulse profiles for GPS1722-36. (a) Profile for no light-bending model,  $SSQ=4.249$ . (b) Profile for light-bending model,  $SSQ=4.210$ .

## CHAPTER 5

### EXO 2030+375:

#### The Luminosity Dependence of Pulse Profile

##### 5.1 Introduction

Parmar et al (1989a)<sup>[24]</sup> discovered a new, transient X-ray pulsar, EXO 2030+375 in May 1985 with the EXOSAT observatory. They followed its evolution through two outbursts. The first outburst occurred between 1985 May and August, and the second occurred in 1985 October. During the first outburst, the 1-20 keV intensity declined by a factor  $\sim 100$  and then within 12 days by another factor of  $\sim 30$  to an intensity close to the limits of detectability. During the second outburst, a series of six flares that recurred quasi-periodically every 3.96 hrs were observed. During each flare the X-ray intensity increased by a factor of  $\sim 6$  over 5-10 minutes and then decayed in an exponential manner over 1.2-2.2 hrs. During five of the flare decays the intensity varied quasi-periodically on a time scale of  $\sim 1000$  s.

The pulse period of 42 s and the orbital period in the range 44.3-48.6 d were found from the EXOSAT observations (Parmar et al, 1989a)<sup>[24]</sup>. The optical companion of EXO 2030+375 was identified as an early-type Be star with  $m_v=19.7$ . From monitoring of the first outburst in the declining phase between May 1985 and August 1985, Parmar et al (1989a)<sup>[24]</sup> found a marked dependence of the rate of change of pulse period ( $\dot{P}$ ) on the X-ray luminosity. Remarkable luminosity-dependent pulse-profile changes were also detected during the course of the decline of the outburst (Parmar et al, 1989b)<sup>[25]</sup>.

A lot of work has been done on the luminosity dependence of pulse properties by comparative studies of different systems (Rappaport & Joss 1979<sup>[29]</sup>; Mason

1977<sup>[30]</sup>; White et al 1983<sup>[23]</sup>). However, before the discovery of the transient X-ray pulsar EXO 2030+375, no study has been carried out over a large luminosity range for an individual pulsar. The previous investigations of luminosity dependence phenomena had been performed on the known  $\sim 30$  accreting X-ray pulsars. The comparative studies showed that, the lower luminosity systems ( $\leq 10^{37}$  ergs s<sup>-1</sup>) have simple sinusoidal-like pulses, whereas the profiles of the higher luminosity systems are more complex, with, in several cases, 180° reversals in the phase of the strongest pulse going from one energy band to another (White et al, 1983<sup>[23]</sup>; Wang & Welter, 1981<sup>[22]</sup>). These comparative studies require a reasonable homogeneous sample, which may not be the case, given the wide range of system geometries and magnetic field strength expected from X-ray pulsars. One way to avoid this problem is to observe the dependence of the pulse profile on luminosity for a single system. The only X-ray pulsars to show large variations in luminosity are transient systems. The observation of pulses from transient systems gives information about an individual pulsar over a large range of luminosity, and provides an alternative way to study the dependence of the pulse period, profile, and spectrum on luminosity.

The appearance of an X-ray transient is caused by a large change in the mass accretion rate onto a compact object and in many cases involves a dynamic range in luminosity of more than  $\sim 1000$ . Luminosity-related changes in the properties of an X-ray source can give insights into the dependence on accretion rate of the emission process.

This chapter will study the luminosity dependence of pulse profiles, and try to use the geometric model of Chapter 2 to explain this phenomenon.

## 5.2 The Observed Pulse Profiles

The observations of a strong luminosity dependence in the pulse profile of EXO 2030+375 are unprecedented for any X-ray pulsar and allow for the first time the possibility of investigating how pulse formation varies with luminosity.

Fig 5-1 and Fig 5-2 show the ten observations of EXO 2030+375 pulse profile during the first outburst (May 18 1985 - August 13 1985). At the maximum observed 1-20 keV luminosity of  $1.0 \times 10^{38}$  ergs  $s^{-1}$  (assuming a distance of 5 kpc; Parmar et al. 1989a<sup>[24]</sup>), the pulse profile shows a smooth asymmetric light curve with two local minima on the trailing edge. The second of the minima is a distinctive notch that becomes both sharper and deeper as the luminosity declines. This notch has been arbitrarily used to define  $\Phi = 0$ . The other minimum also becomes more distinct at lower luminosities such that the pulse maximum at  $\Phi \sim 1.2\pi$  becomes much more symmetric. The notch at  $\Phi = 0$  is clearly present in all but the 1985 July 25 and August 13 profiles. For these two observations, the phase was determined by aligning the single pulses seen at  $\Phi \sim 0.6\pi$  with the narrow pulse seen on 1985 July 10 (Parmar et al, 1989b)<sup>[25]</sup>. Given the similarity in overall shape of the pulses and the evidence for a small feature resembling a notch at  $\Phi \sim 0$  in the 1985 July 25 profile, this seems a reasonable procedure. As the luminosity decreased from the maximum, an interpulse located at  $\Phi \sim 0.6\pi$  appeared and became stronger. By 1985 July 10, when the 1 - 20 keV luminosity had fallen to  $1.2 \times 10^{36}$  ergs  $s^{-1}$ , the inter pulse and the pulse at  $\Phi \sim 1.2\pi$  were of approximately equal strength. This trend continued until August 13 1985, when the pulse at  $\Phi \sim 1.2\pi$  almost entirely disappeared, and the profile became dominated by what had previously been a interpulse. The modulation amplitude of the profile of  $\sim 80\%$  (peak-to-peak) was approximately the same during all observations.

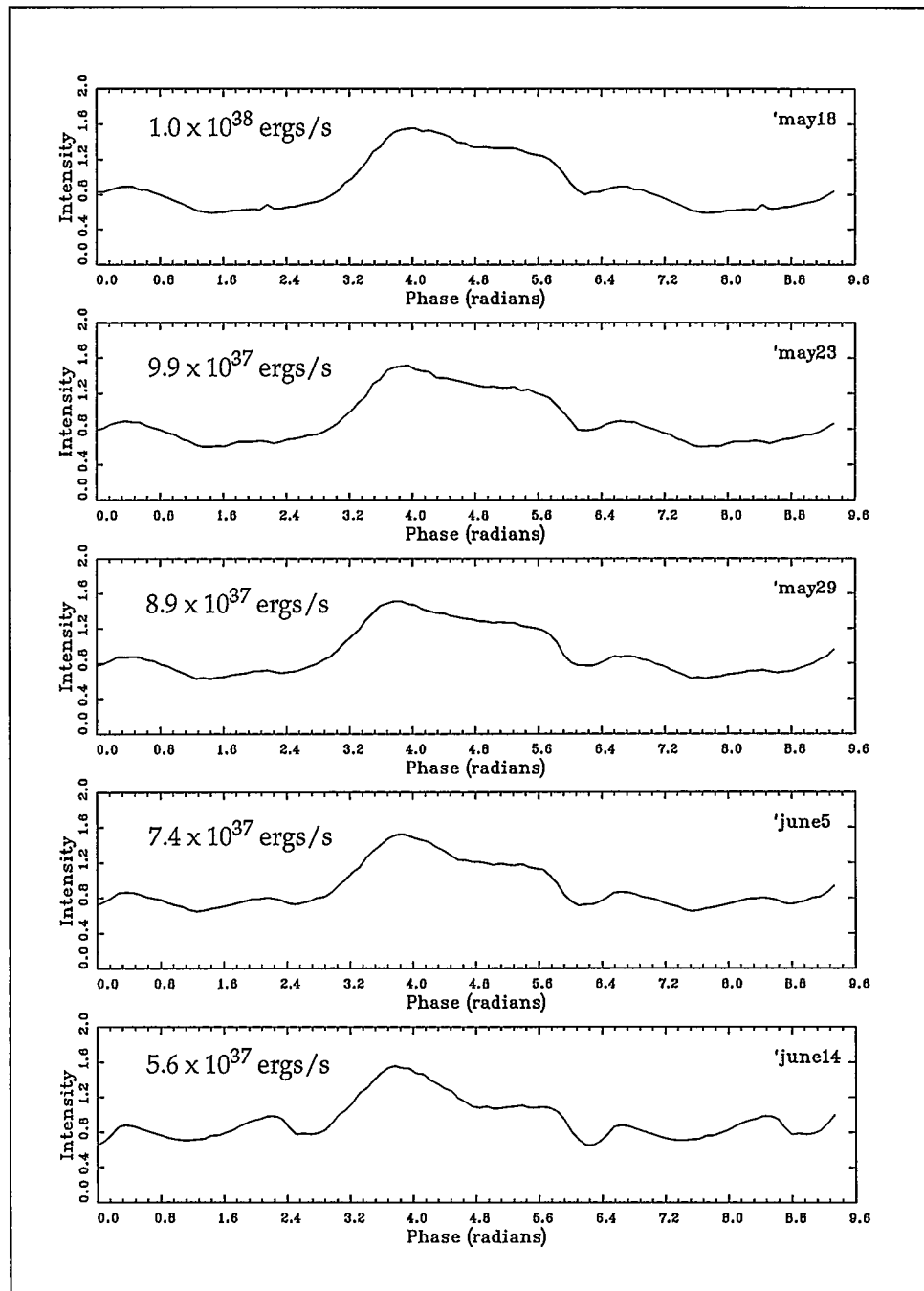


*Fig 5-1* The observed light curves of the first 5 days. 1.5 cycles are shown. The light curves have been aligned in phase so that the sharp notch visible of the main broad peak is centered on  $\Phi = 0.0$ .

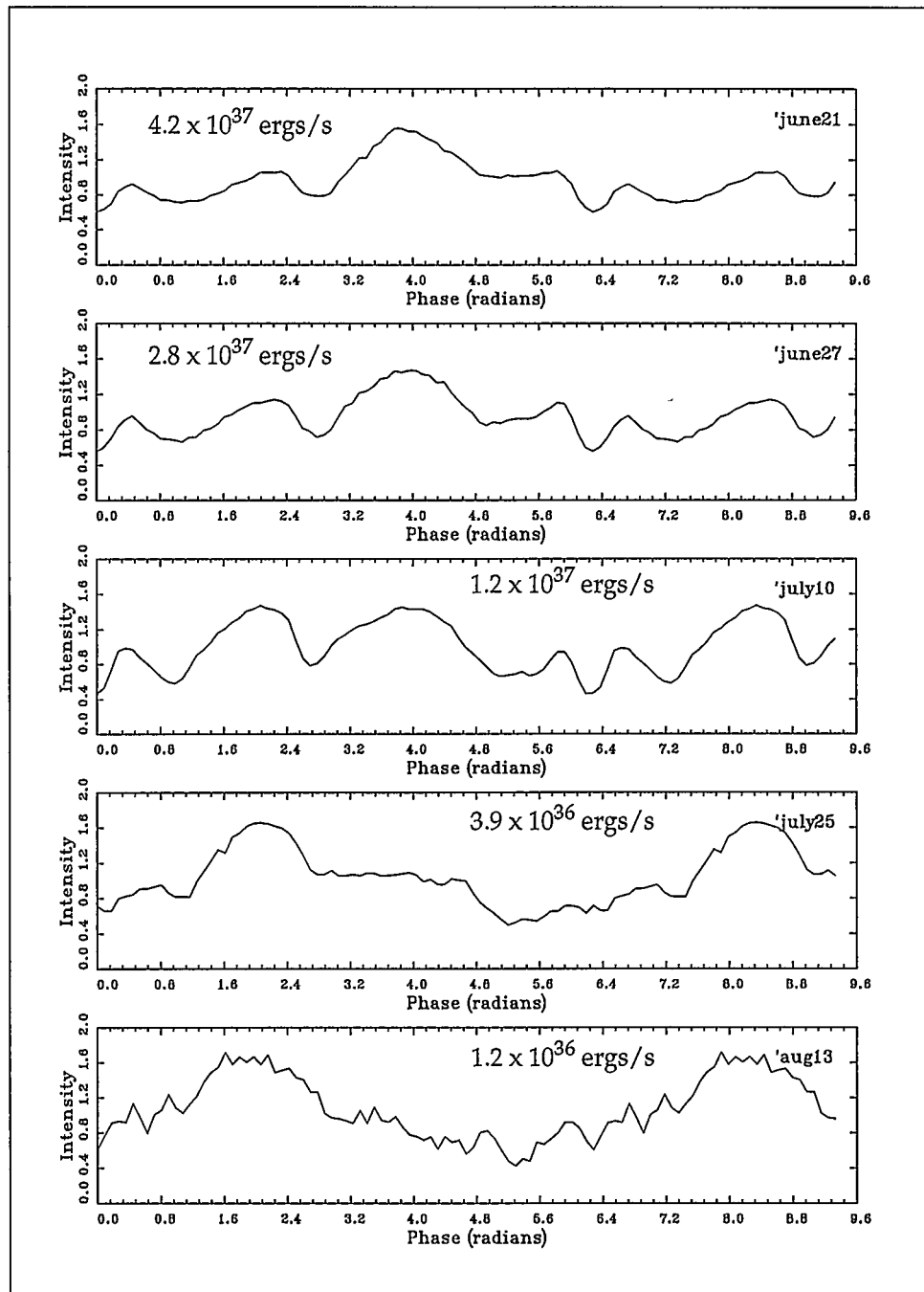


Fig 5-2 The observed light curves of the last 5 days.

### 5.3 Model Assumptions and Pulse Profile Fittings

The geometric model described in Chapter 2 will be used to fit the pulse profiles of EXO 2030+375. The strong luminosity dependence of the pulse profile can test the model by examining the best fit parameters of the different luminosities.

Observations of both of the two outbursts show the same profile dependence on luminosity. As the luminosity of EXO 2030+375 declined, the relative strength of an interpulse, compared to the main pulse, steadily increased, until at the lowest luminosities, their roles were reversed with the interpulse becoming the strongest pulse. In the first outburst, this dependence is on a time scale of weeks, while in the second outburst it is on a time scale of hours. Based on this phenomena, Parmar et al<sup>[25]</sup> ruled out the geometric effects resulting from a precessing neutron star.

We expect that the dependence of the pulse profile on luminosity is caused by the changes in the structure of the accretion disk and its interaction with the magnetosphere of the neutron star. The inflowing plasma will thread different magnetic field lines and fall onto different regions of the neutron star surface (see Fig 2-2 on page 6). The higher luminosity, which is associated with higher accretion rate, thus higher dynamic pressure, will cause the plasma to fall in on closer field lines and flow onto a larger region on the neutron star surface. If this assumption is valid, the luminosity dependent pulse profile can be fitted by varying the size and position of the emission ring while the other parameters are fixed. Refer to Fig 2-4 on page 8 and Fig 2-5 on page 14 for the definitions of the angles. The offset angle  $\theta_o$ , rotational angle  $\theta_r$ , and magnetic angle  $\theta_m$  will be fixed in the fitting program. The emission ring angles  $\alpha_1$ ,  $\alpha_2$ ,  $\beta_1$ ,  $\beta_2$  will then be left free to investigate the dependence of emission region size on the luminosity.

In order to figure out the approximate values which the parameters should be set to, we must first leave all the 10 parameters free and do the fitting for each of the individual dates independently. If the model described in Chapter 2 is suitable for EXO 2030+375, and the assumption in the previous paragraph is proper, we can get good fittings with similar  $\theta_o$ ,  $\theta_r$ , and  $\theta_m$  values for all the 10 observations. Then  $\theta_o$ ,  $\theta_r$ , and  $\theta_m$  can be set to the average values of the 10 days, the fittings can still be good, and the analysis on the variations of the emission ring angles with the luminosity can be performed.

The observed pulse profiles of EXO 2030+375 have more complicated features than the profiles studied in Chapter 4. The EXO 2030+375 profiles have some deep notches and sharp peaks which can not be dealt with by the relatively smooth profiles of the geometric model. These sharp features may result from some other influences such as absorption. So we would like to ignore them in the fittings.

Table 5-1 lists the fitted parameters for the 10 days, using the no light bending model. The pencil beam radiation pattern  $I(\theta') \cos\theta' = A \cos^2\theta'$  is used for all the fittings. The fittings ignored the deep notch around  $\Phi = 0.0$  (the first five and last five data points) for each of the observations (see Fig 5-3 — Fig 5-7). In the table, the first row for each date is the fitting with all the 10 parameters free; the second row is the fitting with  $\theta_o$ ,  $\theta_r$ , and  $\theta_m$  fixed to the average values of the 10 days.

From the Table we can see that, when all the 10 parameters are left free, the model gives quite different values of  $\theta_m$ ,  $\theta_r$ ,  $\theta_o$  for each date. The average values of  $\theta_m$ ,  $\theta_r$ ,  $\theta_o$  are:

Table 5-1 Model parameters for EXO 2030+375

Date <sup>a</sup>	$\theta_m, \theta_r, \theta_o$ <sup>b</sup>	$\alpha_1, \beta_1, \alpha_2, \beta_2$ <sup>b</sup>	SSQ
May 18	1.655, 0.245, 0.872	0.468, 0.844, 0.626, 0.923	0.121
	1.559, 0.392, -0.247	0.821, 1.040, 0.770, 0.856	0.538
May 23	1.288, 0.451, -0.553	0.652, 0.826, 0.674, 0.812	0.116
	1.559, 0.392, -0.247	0.756, 0.994, 0.732, 0.863	0.503
May 29	0.978, 0.288, -1.415	0.805, 0.891, 0.136, 0.927	0.190
	1.559, 0.392, -0.247	0.728, 1.132, 0.727, 0.933	0.434
June 5	0.899, 0.245, -1.51	0.771, 0.829, 0.147, 0.915	0.241
	1.559, 0.392, -0.247	0.757, 0.867, 0.673, 0.751	0.539
June 14	1.908, 0.231, -0.791	1.216, 1.284, 0.211, 0.415	0.256
	1.559, 0.392, -0.247	0.633, 1.032, 0.918, 1.065	0.740
June 21	2.020, 0.209, 0.764	0.000, 0.993, 0.711, 0.774	0.436
	1.559, 0.392, -0.247	0.340, 0.589, 1.076, 1.224	0.624
June 27	1.343, 0.344, -0.790	0.642, 0.714, 0.591, 0.785	0.536
	1.559, 0.392, -0.247	0.626, 0.733, 0.331, 1.373	2.791
July 10	1.845, 0.401, 1.109	0.608, 0.710, 0.702, 0.845	0.953
	1.559, 0.392, -0.247	0.616, 0.726, 0.922, 1.088	3.934
July 25	2.135, 0.691, 0.638	0.331, 0.598, 0.668, 0.785	0.567
	1.559, 0.392, -0.247	0.934, 1.016, 0.666, 0.827	1.500
Aug. 13	2.070, 0.611, 0.147	0.636, 0.751, 0.679, 0.808	1.049
	1.559, 0.392, -0.247	0.693, 0.791, 0.680, 0.816	1.857
<p>a. The first row for each date lists the fittings with all the 10 parameters free. The second row lists the fittings with <math>\theta_m, \theta_r, \theta_o</math> fixed to the average value of the 10 observations. The radiation pattern used in the model is pencil beam <math>\cos^2\theta'</math>.</p>			
<p>b. The unit for angles is radians</p>			

$$\theta_m = 1.559 \pm 0.41 \quad (5-1)$$

$$\theta_r = 0.392 \pm 0.17 \quad (5-2)$$

$$\theta_o = -0.247 \pm 0.90 \quad (5-3)$$

$$(5-4)$$

The errors are calculated from standard deviations:

$$\sigma = \sqrt{\frac{\sum_{i=1}^n (x_i - \bar{x})^2}{n-1}} \quad (5-5)$$

where  $\bar{x}$  is the mean of sample.

Because the model did not give close values for  $\theta_{m'}$   $\theta_{r'}$   $\theta_{o'}$ , the fittings became much poorer after these values were fixed. This is very obvious by observing the significant increase of SSQ in the second row of each date in comparison to the first row. Fig 5-3 — Fig 5-7 show the profile fittings after  $\theta_m$ ,  $\theta_r$ ,  $\theta_o$  are fixed. We can see that the theoretical profiles did not fit the observations very well, especially at lower luminosities, when the observations have sharp multi-peaks.

The light bending model can produce more flexible profiles to fit the sharp features. It gave better fittings to the first four days. However, the sharp profiles from June 14 to July 25 seemed beyond its capability. It was not able to give fittings to these days. The better fittings for the four observations had even bigger standard deviations for  $\theta_{m'}$ ,  $\theta_{r'}$ ,  $\theta_{o'}$ :

$$\theta_m = 1.827 \pm 0.52$$

$$\theta_r = 0.760 \pm 0.28$$

$$\theta_o = -0.646 \pm 0.52$$

So we would like to ignore the light bending effect in the model.

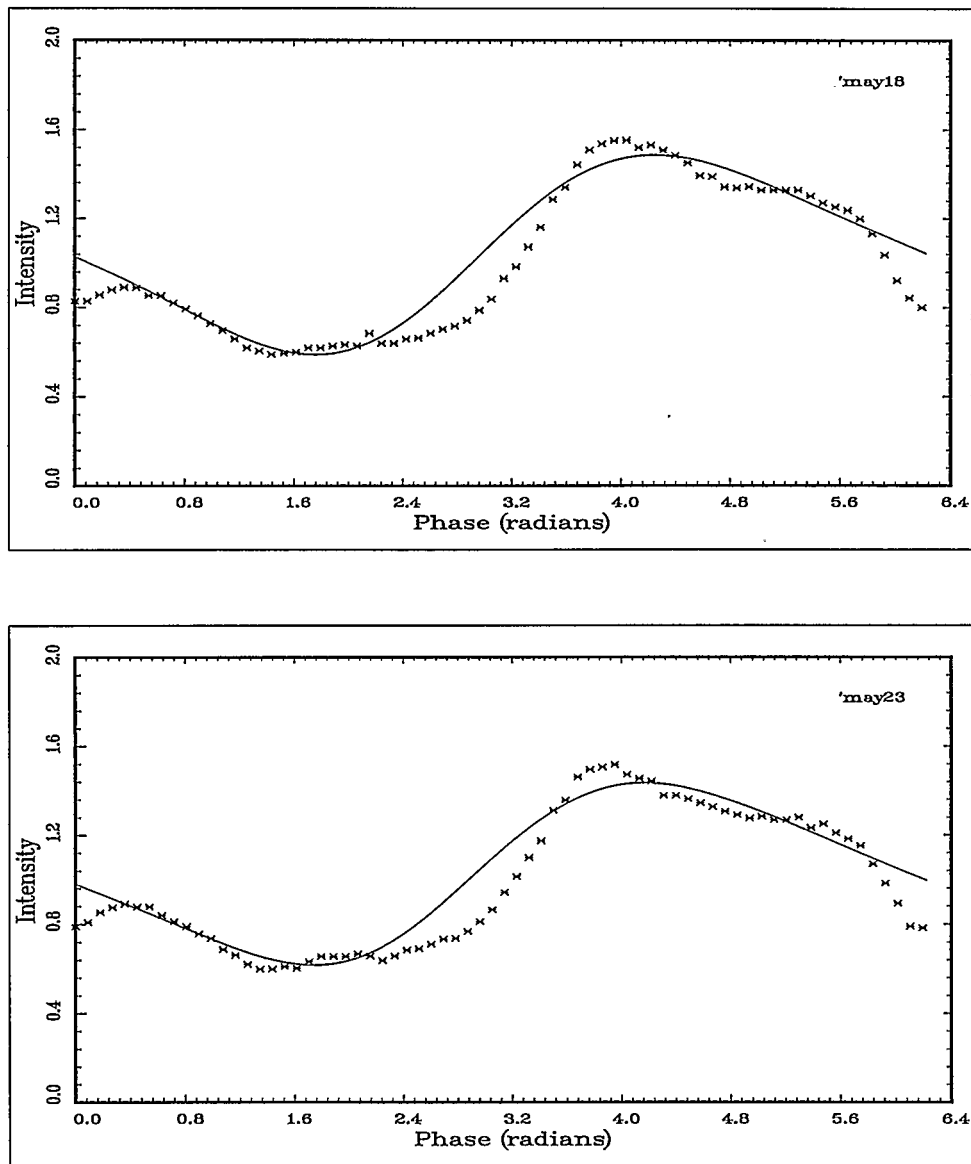


*Fig 5-3* Pulse profile for May 18 and May 23 after  $\theta_m$ ,  $\theta_r$ ,  $\theta_o$  are fixed. The first five and last five data points are ignored in the fitting.

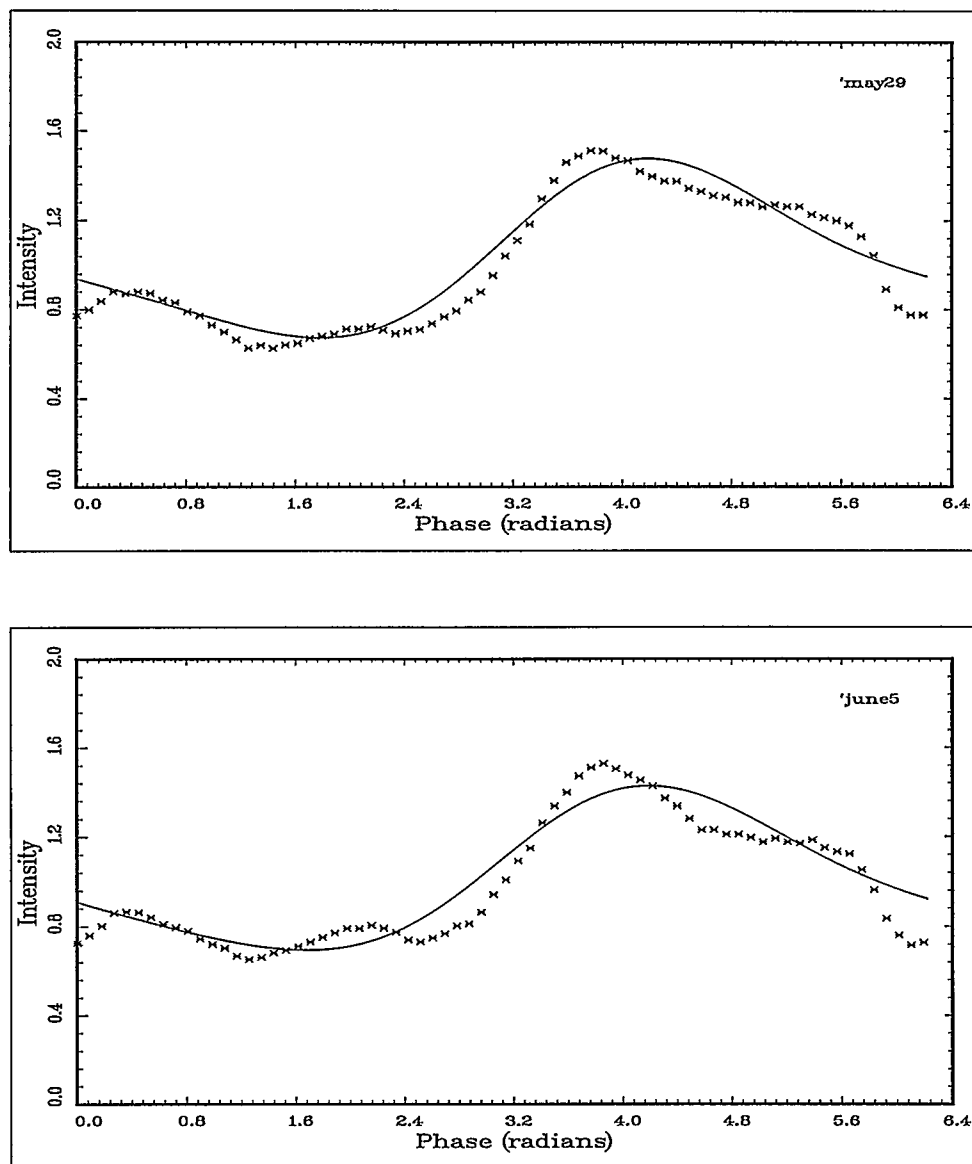


Fig 5-4 Pulse profile for May 29 and June 5 after  $\theta_{mv}$   $\theta_r$   $\theta_o$  are fixed. The first five and last five data points are ignored in the fitting.

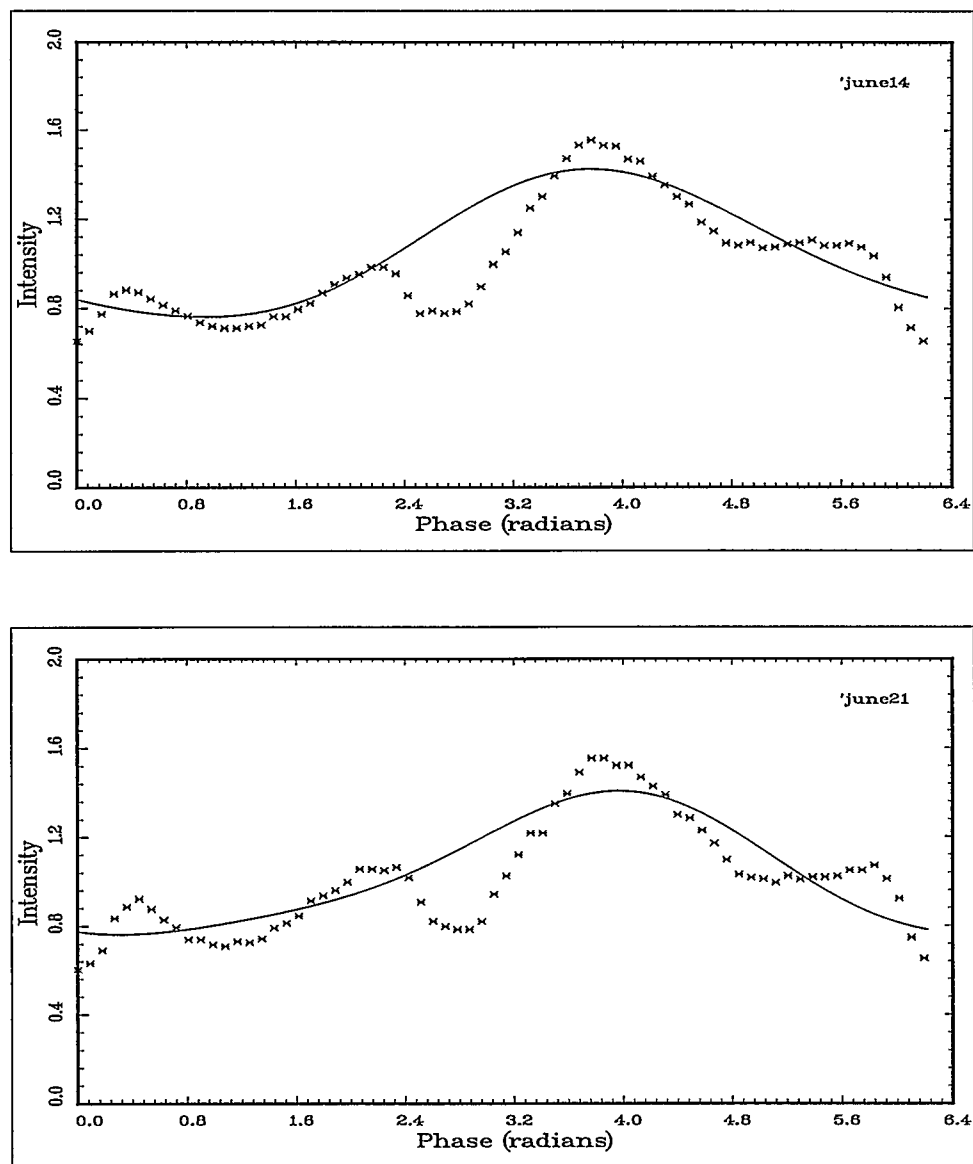
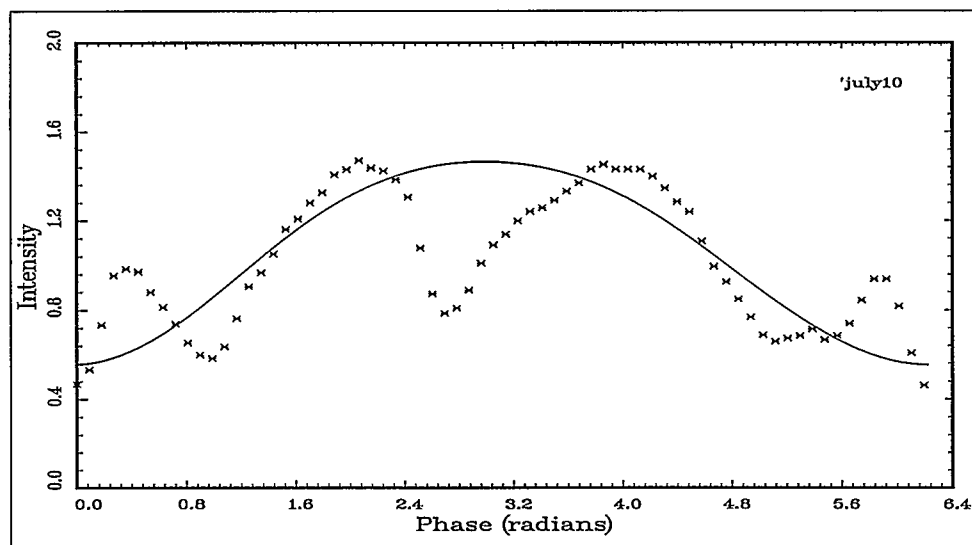
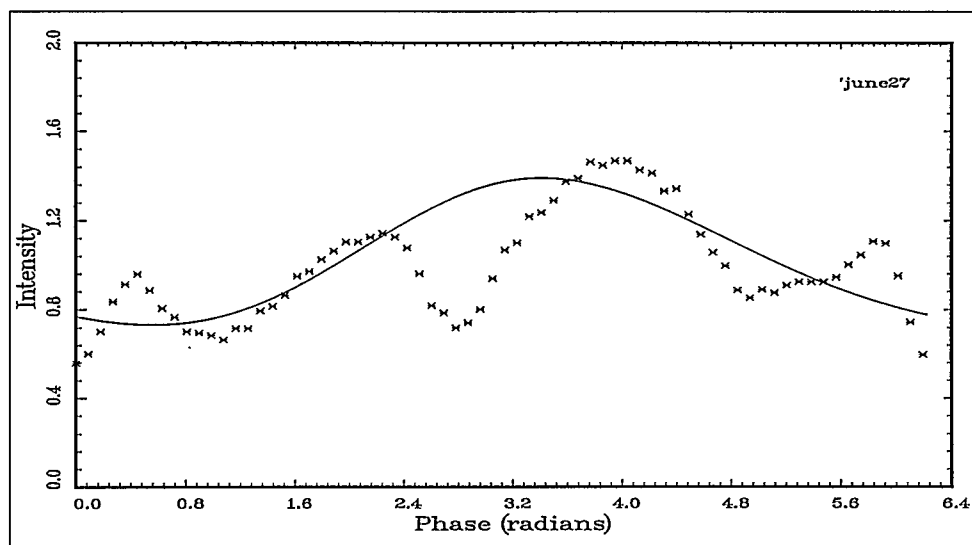


Fig 5-5 Pulse profile for June 14 and June 21 after  $\theta_m$ ,  $\theta_r$ ,  $\theta_0$  are fixed. The first five and last five data points are ignored in the fitting.



*Fig 5-6* Pulse profile for June 27 and July 10 after  $\theta_{nv}$ ,  $\theta_{rv}$ ,  $\theta_o$  are fixed. The first five and last five data points are ignored in the fitting.

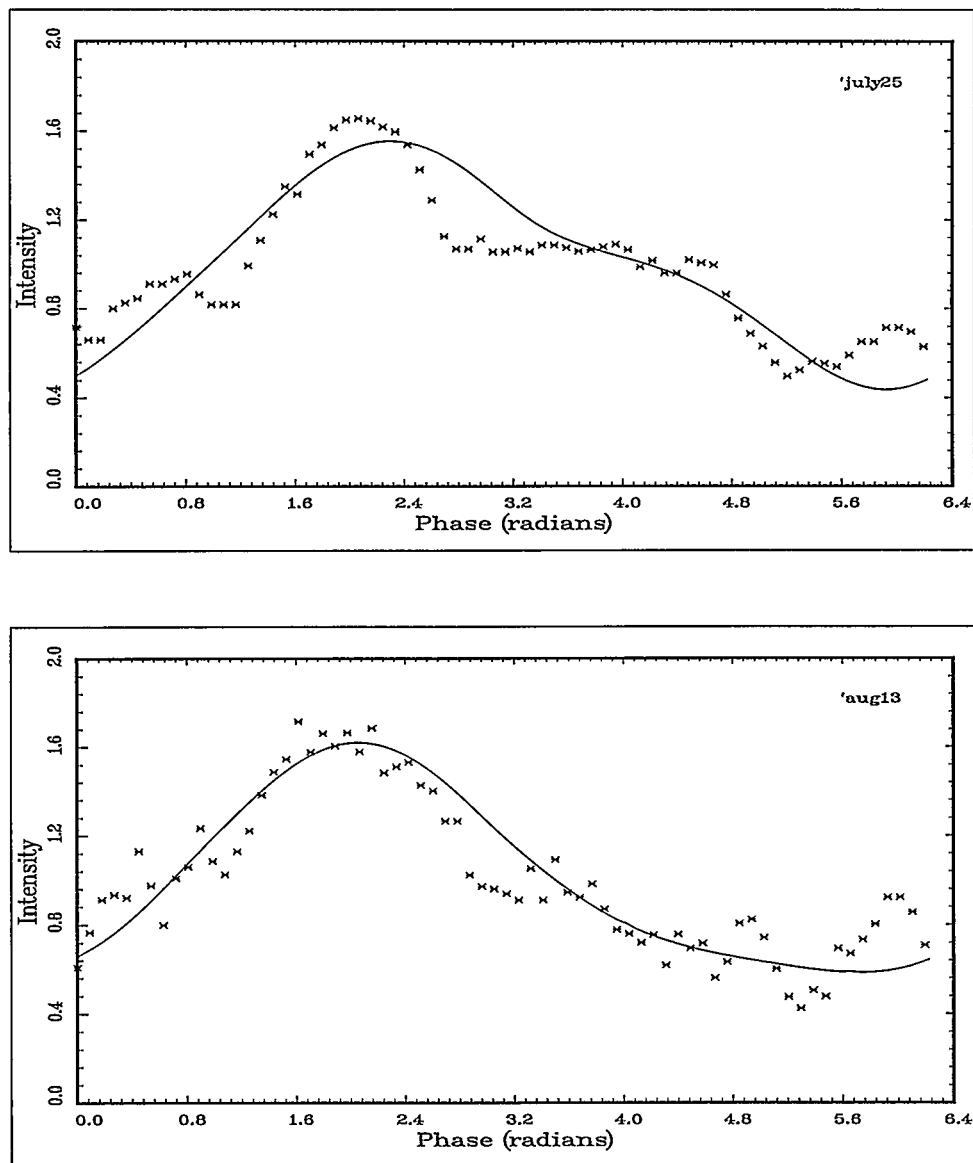
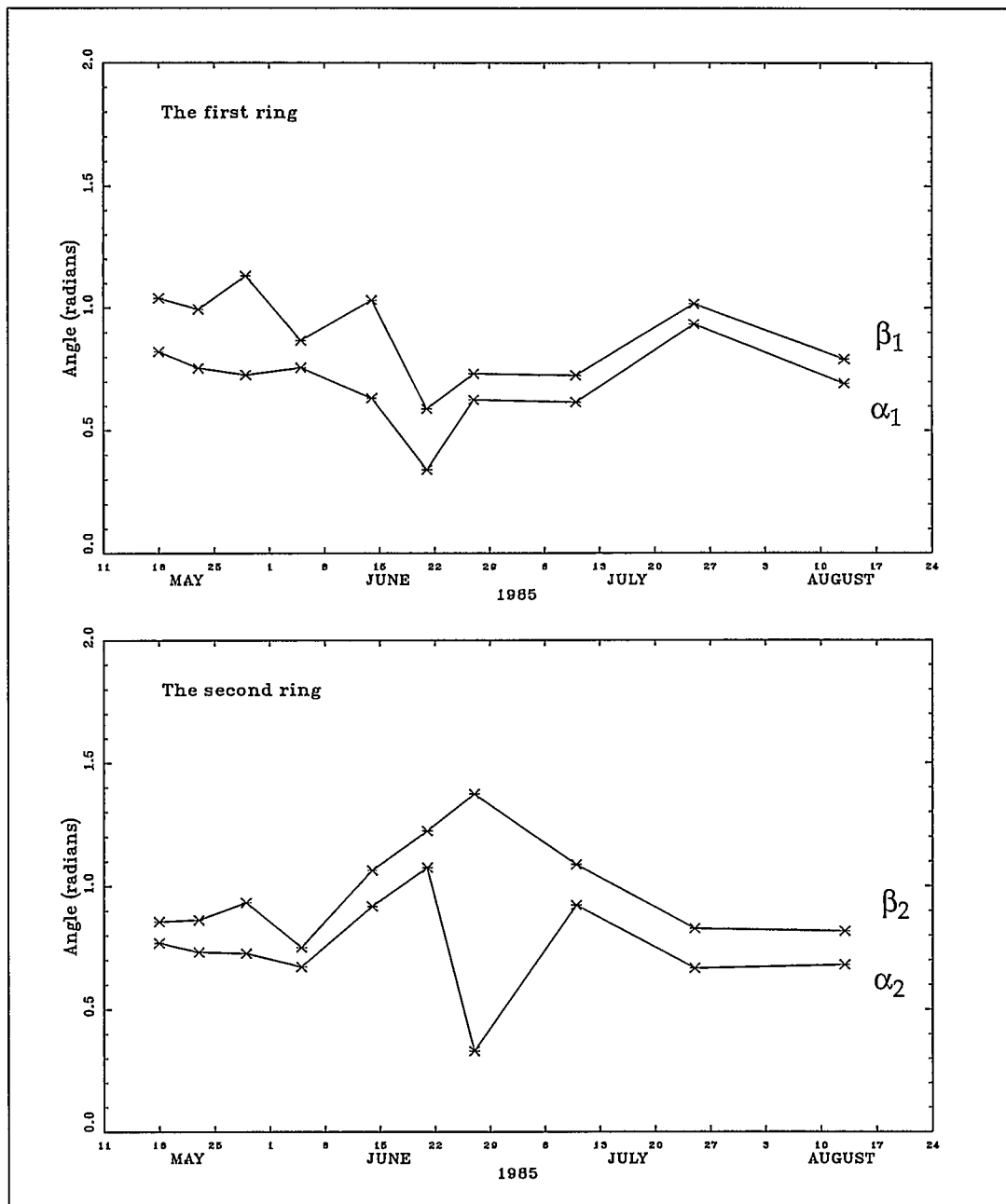


Fig 5-7 Pulse profile for July 25 and Aug. 13 after  $\theta_m$ ,  $\theta_r$ ,  $\theta_o$  are fixed. The first five and last five data points are ignored in the fitting.



*Fig 5-8* Emission ring angles vs. dates for both rings. Luminosity is decreasing with time. No regularity is shown on the positions and widths of the rings.

Given the bad fittings of emission ring angles  $\alpha_1$ ,  $\beta_1$ ,  $\alpha_2$ ,  $\beta_2$ , the study of the correlation between the luminosity and emission rings can not give satisfactory results. Fig 5-8 plots the emission ring angles on different dates. The y-coordinates of the points show the positions of the rings from the magnetic poles; the change in the distance between the two lines implies the change in the ring width with dates. Because the luminosity is decreasing with time, according to the model assumptions we made before, the rings are expected either to go closer to the poles or become narrower, to make a smaller emission region for lower luminosity. Nevertheless, Fig 5-8 does not show the regularity we expected on the positions and widths of the rings.

However, the analysis of the relation between luminosity and the solid angle of the emission region (sum of the two rings) seems more optimistic. Table 5-2 lists the values of luminosity and emission region size for each observation, and Fig 5-9 is a plot of them. The straight line in the graph, though not a good fit to the points, shows a trend of luminosity increasing with emission region size, as the model assumptions indicate.

**Table 5-2 Luminosities and emission region sizes of EXO 2030+375**

Date	Luminosity (ergs/s)	Solid angle of emission region: $\Omega$	Date	Luminosity (ergs/s)	Solid angle of emission region: $\Omega$
May 18	$1.0 \times 10^{38}$	1.494	June 21	$4.2 \times 10^{37}$	1.547
May 23	$9.9 \times 10^{37}$	1.736	June 27	$2.8 \times 10^{37}$	5.127
May 29	$8.9 \times 10^{37}$	2.973	July 10	$1.2 \times 10^{37}$	1.307
June 5	$7.4 \times 10^{37}$	0.825	July 25	$3.9 \times 10^{36}$	1.116
June 14	$5.6 \times 10^{37}$	2.612	Aug 13	$1.2 \times 10^{36}$	0.999

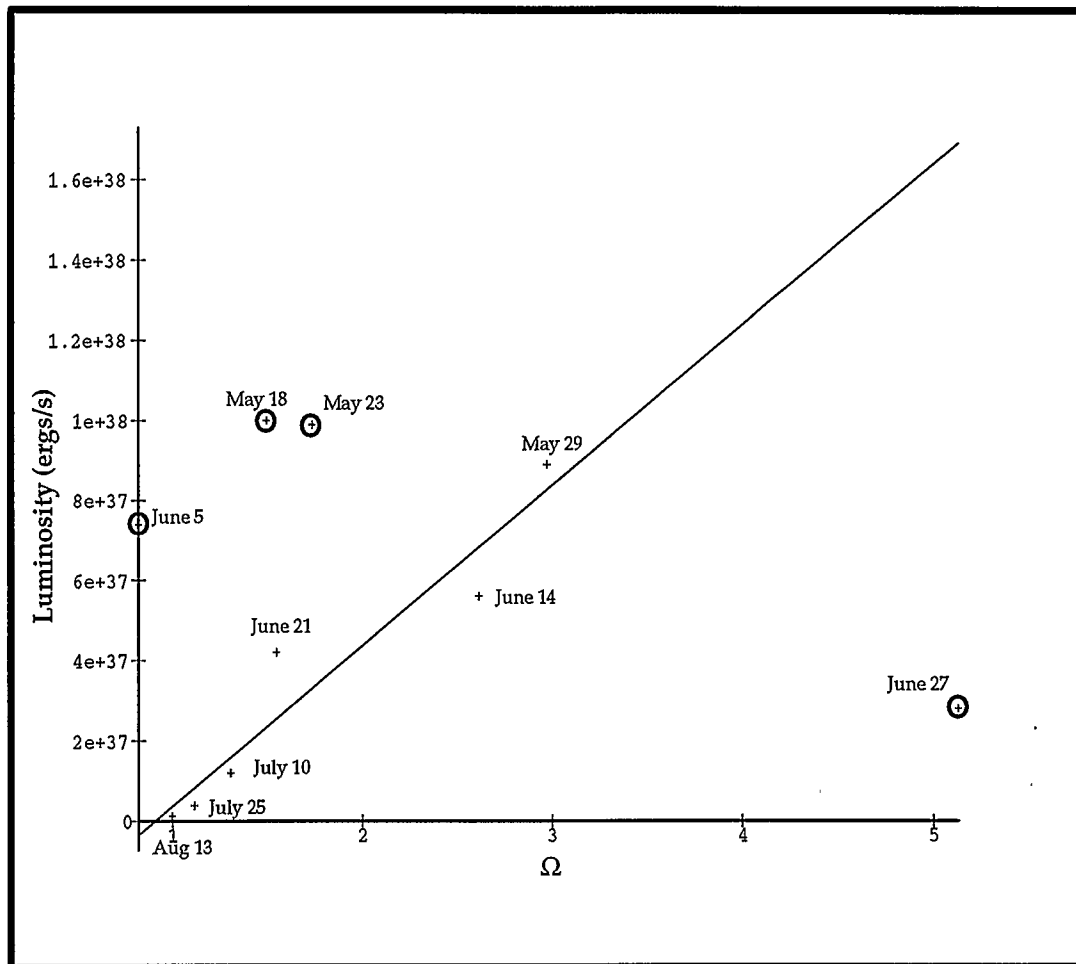


*Fig 5-9* Luminosity vs.  $\Omega$ . The equation for the straight line is:  $L = 0.401 \times 10^{38} \Omega - 0.366 \times 10^{38}$ . Although the four circled points scatter quite far away from the line, the other six points do follow the trend of the line, displaying an approximate proportional relation between luminosity and emission region size, which is consistent with the model assumptions.

#### 5.4 Fan Beam Radiation Pattern

For many viewing directions, a fan beam can produce sharp features in pulse profile, as the fan beam rotates behind the horizon of the neutron star (Wang and Welter, 1981)<sup>[31]</sup>. Considering the sharp features in the EXO2030+375 profiles, a fan beam pattern may be more suitable for this pulsar.

When the plasma encounters the neutron star surface, a radiative shock may occur, producing a “pillbox” emission region (see Fig 2-3 on page 7). Radiation is emitted sideways, giving a fan beam pattern. By Wang and Frank (1981)<sup>[32]</sup>, as the luminosity decreases, the height of the radiative shock will decrease. At some luminosity, possibly around  $10^{37}$  ergs/s, the emission region may switch from a cylindrical “pillbox” to a thin slab, thus the radiation switches from fan beam to pencil beam.  $10^{37}$  ergs/s is in the range of luminosity observed from EXO 2030+375. The almost  $180^\circ$  switch in phase of the main pulse might be associated with a switch from fan beam to pencil beam direction.

Assuming the accretion column is a thin-walled hollow funnel, the configuration of the fan beam model is quite complicated. (Fig 5-10). Though qualitative calculations of the fan beam model had been performed by several authors (e.g. Mészáros 1984<sup>[6]</sup>, Parmar et al, 1989<sup>[24]</sup>), detailed fits to establish the viewing geometry have not, in general, been made, except for the paper of Riffert et al (1993)<sup>[17]</sup>. In that paper, they used the same parameters defined in Fig 2-4 on page 8 and Fig 2-5 on page 14 to describe the geometry of the fan beam model, and applied intensity distribution:  $I = A \sin^3 \theta$  on the model. The emission from a radiation column, of course, can not be simulated by a polar cap or ring with just a different beam pattern. This is a crude approximation for columns that are small both in height and width.

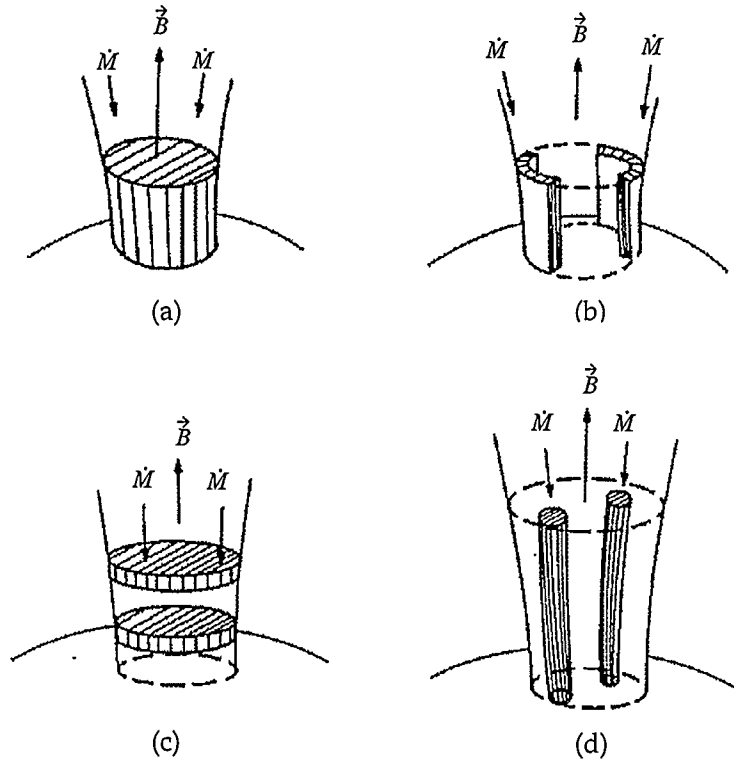


*Fig 5-10* Possible transverse geometries of the emission region at polar cap: (a) Filled funnel. (b) Hollow sectional funnel. (c) Pancaked. (d) Spaghettis. (Adopted from Mészáros, P., 1984)<sup>[6]</sup>.

However, this approximation doesn't work well for EXO 2030+375. With the radiation pattern  $I = A \sin^3 \theta$ , the program gives out quite bad fittings. Equations 5-6 — 5-8 below give the mean and standard deviations of  $\theta_m$ ,  $\theta_r$ ,  $\theta_o$ . we can see that the standard deviations of  $\theta_m$ ,  $\theta_r$ ,  $\theta_o$  are very big. Thus it is meaningless to fix them to analyze the luminosity dependence of emission rings.

$$\theta_m = 0.970 \pm 0.89 \quad (5-6)$$

$$\theta_r = 0.234 \pm 0.29 \quad (5-7)$$

$$\theta_o = -0.615 \pm 1.02 \quad (5-8)$$

These results show that the pencil beam model is better than the simple geometry fan beam model, even though neither described the pulse shape of EXO2030+375 adequately.

### 5.5 Conclusion

The fittings of the geometric model to the observations of EXO 2030+375 are not good enough to test the assumption of the luminosity dependence of the properties of the emission rings. EXO 2030+375 is still a mystery. A better geometry figure may improve the fittings and make it possible to investigate the luminosity dependence. From past experience, sometimes simple changes in the model geometry make large differences in the pulse profiles and quality of the fittings. However, no attempt has yet been done to find a good approximation to the fan beam geometry and work out the mathematics.

## CHAPTER 6

### CONCLUSION

#### 6.1 Summary

In this thesis, a geometric model for pencil beam radiation was used to fit the observed pulse profiles. The model assumed two offset emission rings on the neutron star surface. The radiation is emitted uniformly over the entire ring area. The local emission pattern of the intensity is  $I \cos \theta' \propto \cos^n \theta'$ , with  $n$  being either 2 or 4, where  $\theta'$  is the angle between the emission light and the local normal of the neutron star surface. The effect of general relativity was incorporated into the model through a simple analytical formula of the light bending effect given in Chapter 3.

The light bending model was successful for the 7 pulsars studied in Chapter 4. Comparing with the no light bending model, the light bending model produced sharper features in the profile to give the observation a better fitting. Also the derived parameters gave smaller emission regions as theoretically expected.

However, the pencil beam emission model could not give a satisfactory answer to the luminosity dependence of pulse profiles of EXO2030+375. The model did not give good fitting to each individual observation, so the physical meaning of the fitted parameters are doubtful. The assumption that higher luminosity is corresponding to a larger emission region on the neutron star surface was only poorly demonstrated by the derived emission ring parameters. A simple approximation was made that the fan beam model has the same geometry picture as the pencil beam model, with emission pattern  $I \propto \sin^3 \theta'$ . This approximation turned out to be too crude to improve the fittings. More detail work needs to be done to construct a better fan beam model.

## 6.2 Future Work

A simple approximation for the emission region of the fan beam model may start with two very thin columns sticking out from two magnetic poles (see Fig 6-1). These two columns can be offset and have different heights.

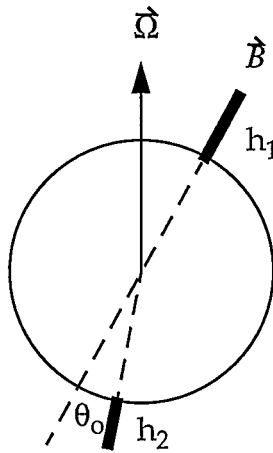


*Fig 6-1* A simple geometry approximation for fan beam model:  
Two offset thin columns, with different height:  $h_1, h_2$ .

The column parameters  $h_1$  and  $h_2$  will replace the emission ring parameters  $\alpha_1, \beta_1, \alpha_2, \beta_2$ , but all the other geometry parameters are the same as those defined in Fig 2-4 on page 8 and Fig 2-5 on page 14. Then we can have the following equation to replace equation (2-20) on page 14:

$$f = f \left( \underline{\theta}_0, \underline{\theta}_m, \underline{\theta}_r, \underline{\phi}_{ro}, \underline{h}_1, \underline{h}_2, \underline{\Phi}_0, \underline{\Phi} \right) \quad (6-1)$$

A suggestion for future work would be working out the mathematics of this

model, and applying it to EXO2030+375. A proper radiation pattern must be chosen for radiation from the emission column. The light bending effect can also be incorporated into the model. If it can give better fittings to the sharp profiles of EXO2030+375, physically meaningful parameters will be derived. Then the relation between the luminosity and the emission column parameters can be studied.

## Appendix

### The Analytical and Numerical Integrations in the Fitting Program

#### 1 . Structure of the fitting program

The soul of the fitting program is the IMSL routine DUNLSF (Double precision). DUNLSF uses a modified Levenberg-Marquardt method to solve nonlinear least squares problems. The problem is stated as follows:

$$\min_{x \in \mathfrak{R}^n} \frac{1}{2} F(x)^T F(x) = \frac{1}{2} \sum_{i=1}^m f_i(x)^2 \quad (\text{A-1})$$

where  $m \geq n$ ,  $F: \mathfrak{R}^n \rightarrow \mathfrak{R}^m$ , and  $f_i(x)$  is the  $i$ -th component function of  $F(x)$ . In this case,  $m$  is the number of observation data points, which is different for individual pulsars, ranging from 10-60;  $n$  is the number of free parameters, which is 10 for the most general model (see Table 2-1 on 2-1 on page 15).  $F(x)$  is defined as the difference between the observation and the theoretical calculation of  $f(\theta_1, \phi_1)$  (equation 2-3). Equation 2-20 on page 14 shows  $f$  as a function of the 10 free parameters and the observation phase. The observational data is the flux vs. phase. So the flux calculated from equation 2-20 can be directly compared with the observation. With a set of initial guesses for the free parameters (a vector of length  $n$ ), DUNLSF will try to find out the approximate solution of the free parameter vector which can minimize equation A-1. By this way, the theory gets its closest fit to the observation.

Fig A-1 shows how the program works:

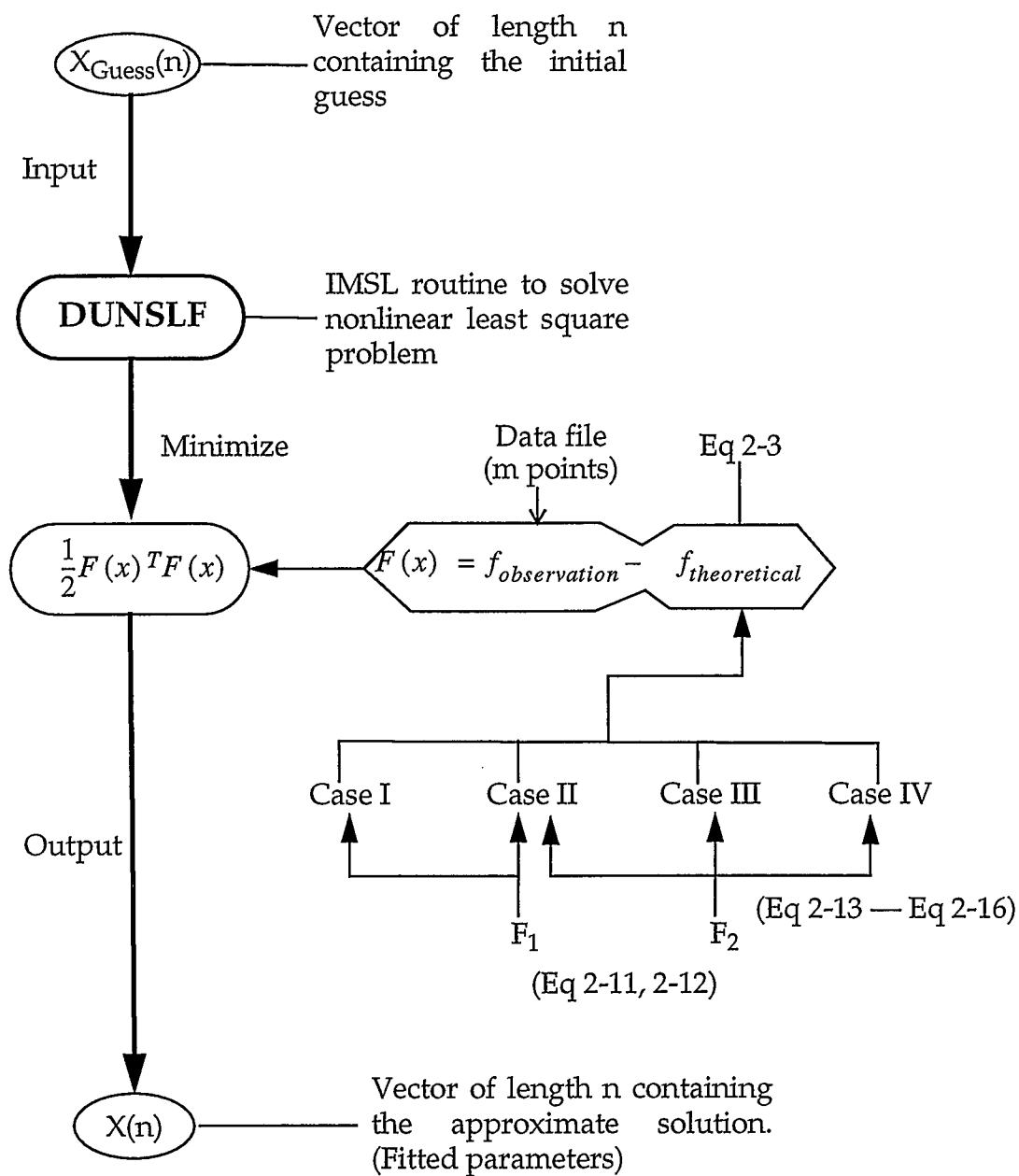


Fig A-1 Structure of the fitting program

## 2 . Overview of the equations

Fig A-2 is an overview of the equations for the geometric model described in Chapter 2. This chart shows the process to evaluate the theoretical flux.

- a. Equation <4> is the light bending equation 3-1. This equation gives the relation between  $\cos\theta'$  and  $\cos\theta_0'$ , thus the relation between  $\theta'$  and  $\theta_0'$ .
- b. Equation <3> (eq. 2-4) gives the dependence of  $\theta_0'$  on the spherical polar coordinates  $(\theta'', \phi'')$ .
- c. Combining equation <4> with equation <3> we can obtain the relation between  $\theta'$  and  $(\theta'', \phi'')$ .
- d. With this relation substituted into radiation pattern equation <2> (the combination of equation 2-1 and equation 2-2), the integration for angular distribution equation <1> (eq. 2-3) can be done.

In the fitting program, the evaluation of the theoretical flux will be performed hundreds of times, and takes most of the CPU time. Speeding up of this process is the key to speed up the whole program.

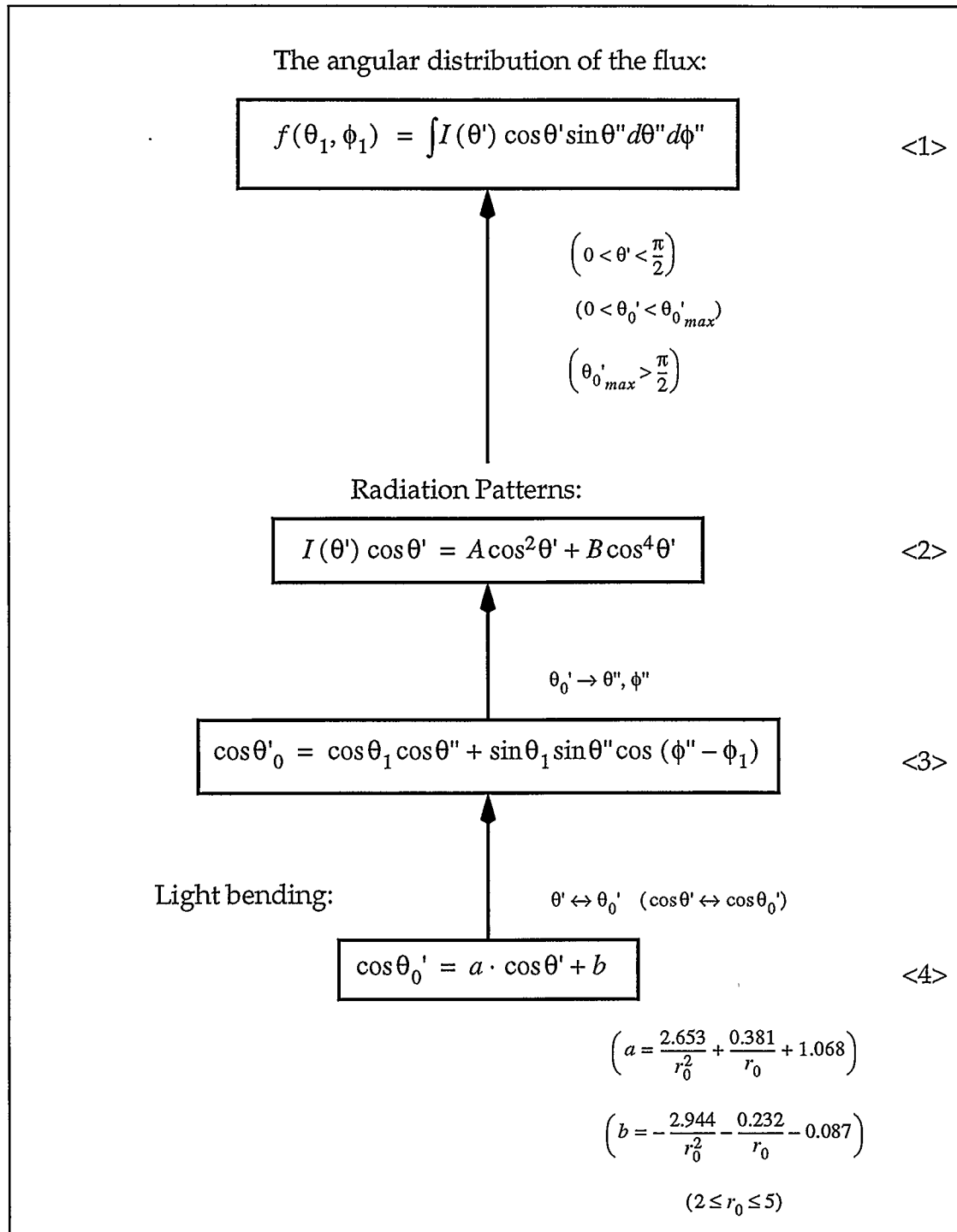


Fig A-2 Equation overview for the Geometric Model.

### 3 . The analytical formulae for the no light bending model

For the no light bending model, the analytical calculation of  $f(\theta_1, \phi_1)$  (equation 2-3) had been carried out by Mr. G. R. Young with the aid of MACSYMA (MACSYMA is a registered trademark of the Symbolics Inc.). Equation A-2 and A-3 show the results of the two integrations of equation 2-11 and 2-12 (see Leahy 1991)<sup>[2]</sup>.

$$\begin{aligned}
 F_1(\theta_1, \alpha, \beta) &= \int_{\alpha}^{\beta} d\theta'' \int_0^{2\pi} I(\theta') \cos\theta' \sin\theta'' d\phi'' & (A-2) \\
 &= \pi \left[ \frac{1}{3} (\cos^3\beta - \cos^3\alpha) + \cos\alpha - \cos\beta \right] \sin^2\theta_1 + \\
 &\quad \frac{2\pi}{3} (\cos^3\beta - \cos^3\alpha) \cos^2\theta_1
 \end{aligned}$$

$$\begin{aligned}
 F_2(\theta_1, \alpha, \beta) &= 2 \int_{\alpha}^{\beta} d\theta'' \int_{\phi_1}^{(\arccos[-\cot\theta_1 \cot\theta''] + \phi_1)} I(\theta') \cos\theta' \sin\theta'' d\phi'' & (A-3) \\
 &= -\cot\theta_1 \left\{ (2 - 3\sin^2\theta_1) \left[ -(\cot^2\theta_1 + 1) \right. \right. \\
 &\quad \times \arcsin\left( \frac{\cot^2\theta_1}{\sqrt{(\cot^2\theta_1 + 1) |\cot\theta_1| |\sin\theta''|}} \right) \\
 &\quad \left. \left. - |\cot\theta_1| \sqrt{(\cot^2\theta_1 + 1) \sin^2\theta''} \right] \right\} \\
 &\quad - \sin^2\theta_1 \arctan\left( \frac{\sqrt{(\cot^2\theta_1 + 1) \sin^2\theta''}}{\cot\theta_1} \right) \\
 &\quad + \sin^3\theta_1 |\sin^3\theta''| \left( 1 + \cot^2\theta_1 - \frac{\cot^2\theta_1}{\sin^2\theta''} \right)^{3/2} \\
 &\quad - \frac{2\pi}{3} \cos^2\theta_1 \cos^3\theta'' + \pi \sin^2\theta_1 \left( \frac{1}{3} \cos^3\theta'' - \cos\theta'' \right) \Big|_{\alpha}^{\beta}
 \end{aligned}$$

Where the radiation pattern is:

$$\begin{aligned} I(\theta') \cos\theta' &= \cos^2\theta' = \cos^2\theta_0' & (A-4) \\ &= [\cos\theta_1 \cos\theta'' + \sin\theta_1 \sin\theta'' \cos(\phi'' - \phi_1)]^2 \end{aligned}$$

for the no light bending case.

For the case of  $\cos^4\theta'$  radiation pattern, the integration results of  $F_1$  and  $F_2$  are much lengthier expressions, which are still analytic in form.

These formulae were tested with the results of the numerical integrations of IMSL routines and proved to be correct.

The analytical formulae, though lengthy and complicated, are fast in the fitting programs. The typical CPU time is seconds.

#### 4 . The numerical integration for the light bending model

For general relativity light bending, a simple linear equation (3-1) was found to replace the complicated integration equation (2-5) (please see Chapter 3). With this linear equation (3-1), the incorporation of light bending effect into the fitting program becomes practical, and several ways to speed up the program were found.

After the light bending effect is included in the emission model,  $I(\theta') \cos\theta'$  in the integrands of  $F_1$  and  $F_2$  becomes:

$$\begin{aligned}
I(\theta') \cos \theta' &= \cos^2 \theta' & (A-5) \\
&= \left[ \frac{1}{a} (\cos \theta_0' - b) \right]^2 \\
&= \left[ \frac{1}{a} (\cos \theta_1 \cos \theta'' + \sin \theta_1 \sin \theta'' \cos (\phi'' - \phi_1) - b) \right]^2
\end{aligned}$$

Where  $a, b$  are determined by equation 3-2, 3-3 on page 21.

In this case, no analytical form for  $f(\theta_1, \phi_1)$  can be found. Numerical integrations have to be used in the programming.

First, an IMSL routine DTWODQ was employed to do the two-dimensional integration. In this way, programming is convenient. One can try different radiation patterns  $I(\theta') \cos \theta'$  by just changing one line in the code. However, these two-dimensional numerical integrations turned out to be very slow, with typical CPU time as long as hours. This is remarkably inefficient, especially when a lot of trials of initial value sets have to be used to get the best possible results.

Then, the analytical result of  $F_1(\theta_1, \alpha, \beta)$  was used in the program:

$$\begin{aligned}
F_1(\theta_1, \alpha, \beta) &= \frac{\pi}{a^2} (\cos \alpha - \cos \beta) \cdot \{ 2b^2 + 1 - \cos \theta_1 & (A-6) \\
&\quad + (\cos \alpha + \cos \beta) \cdot [-2b \cdot \cos \theta_1 + (\cos^2 \theta_1 - 3) \cos \alpha] \\
&\quad + (\cos^2 \theta_1 - 3) \cdot \cos^2 \beta \}
\end{aligned}$$

However,  $F_2(\theta_1, \alpha, \beta)$  is more important than  $F_1(\theta_1, \alpha, \beta)$  in the program. We can see this from Fig A-1,  $F_2$  exists in all of the cases except Case I, which is a relatively rare case (the entire ring is visible). Especially when two rings are

considered, this case never really exists for both of the two rings. Because it is impossible for two rings to be entirely visible to the observer simultaneously,  $F_1$  is always bound with  $F_2$ , and never appears in the computing alone. So the analytical results of  $F_1$  did not speed up the program significantly.

Finally, an analytical calculation for the integral over  $\phi''$  was performed for  $F_2$ , thus  $F_2$  can be expressed as a one dimensional integration:

$$\begin{aligned} F_2(\theta_1, \alpha, \beta) &= 2 \int_{\alpha}^{\beta} d\theta'' \int_{\phi_1}^{(\arccos[-\cot\theta_1 \cot\theta''] + \phi_1)} I(\theta') \cos\theta' \sin\theta'' d\phi'' \quad (\text{A-7}) \\ &= 2 \int_{\alpha}^{\beta} \sin\theta'' d\theta'' \left[ C(A-D)^2 + \frac{1}{2}B^2C + B \sin C \left( 2A + \frac{1}{2}B \cos C - 2D \right) \right] \end{aligned}$$

Where:

$$A = \frac{1}{a} \cos\theta_1 \cos\theta''$$

$$B = \frac{1}{a} \sin\theta_1 \sin\theta''$$

$$C = \arccos[-\cot\theta_1 \cot\theta'']$$

$$D = \frac{b}{a}$$

IMSL routine DQDAWQ is then employed to do the one dimensional numerical integration. This one dimensional integration is much faster than the two dimensional one. It speeds up the program by tens of times, depending on the input initial value sets for the fitting. The typical CPU time of the code with the analytical result for  $F_1$  and one dimensional integration for  $F_2$  is minutes. This dramatic decrease in CPU time make it much more convenient to try different initial value sets for the parameters to get the best possible fittings.

## REFERENCES

- [1] Pringle, J. , & Reess, M., 1972, *Astr.Astrophysics.*, **21**, 1
- [2] Leahy, D. A., 1991, *Mon. Not. R. astr. Soc.*, **251**, 203
- [3] Davidson, K. & Ostrike, H., 1973, *ApJ*, **179**, 585
- [4] Lamb, F. K., Pethick, C.J., & Pines, D., 1973, *ApJ*, **184**, 271
- [5] Ghosh, P., & Lamb, F., 1979, *ApJ.*, **234**, 296
- [6] Mészáros, P., 1984, *Space Science Review*, **38**, 325
- [7] Mészáros, P., & Nagel, W., 1985, *ApJ*, **299**, 138
- [8] Leahy, D. A., 1990, *Mon. Not. R. astr. Soc.*, **242**, 188
- [9] Riffert, H., & Mészáros, P., 1988, *ApJ*, **325**, 207
- [10] Landau, L. D., 1932. *Phys. Abh. Sov. Union*, **1**, 285
- [11] Badde, W. & Zwicky, F., 1934a, *Phys. Rev.*, **45**, 138
- [12] Badde, W. & Zwicky, F., 1934b, *Proc. Nat. Acad. Sci.*, **20**, 254
- [13] Oppenheimer, J. R. & Volkoff, G. M., 1939, *Phys. Rev.*, **55**, 374
- [14] Shapiro, S. L., & Teukosky, S. L., 1983, *Black Holes, white Dwarfs, and Neutron*

*Stars*, ( New York: Wiley - Intersciences)

- [15] Misner, C. W., Thorne, K. S., and Wheeler, J. A., 1973, *Gravitation*,  
(San Francisco: Freeman)
- [16] Mészáros, P., 1992, *High-Energy Radiation from Magnetized Neutron stars*, (The  
University of Chicago Press)
- [17] Riffert, H., Nollert, H.-P., Kraus, U., & Ruder, H., 1993, *ApJ*, **406**, 185
- [18] Blair, D. G., and Candy, B. N., 1985, *Monthly Notices Roy. Astron. Soc.*, **212**, 219
- [19] Corbet, R. H. D., 1986, *Monthly Notices Roy. Astron. Soc.*, **220**, 1047
- [20] Stella L., White, N. E., & Rosner, R., 1986, *ApJ*, **308**, 669
- [21] Nagase, F., 1989, *Publ. Astron. Soc. Japan*, **41**, 1
- [22] Wang, Y., & Welter, G., 1981, *Astr. Astrophysics.*, **102**, 97
- [23] White, N., Swank, J., & Holt, S., 1983, *ApJ*, **270**, 711
- [24] Parmar, A. N., White, N. E., & Stella, L., 1989a, *ApJ*, **338**, 359
- [25] Parmar, A. N., White, N. E., & Stella, L., 1989b, *ApJ*, **338**, 373
- [26] Ceo, M. J., Hanson, C. G., & Lonmore, A. J., *IAU Circular*, No. **4096**, 1985
- [27] Ceo, M. J., Lonmore, A. J., Payne, B. J., & Hanson, C. G., 1988, *Mon. Not. R.*

*astr. Soc.*, **232**, 865

[28] Motch, C., & Janot-Pacheco, E., 1987, *Astr.Astrophysics.*, **182**, L55

[29] Rappaport, S., & Joss, P. C., 1977, *Nature*, **266**, 683

[30] Mason, K. O., 1977, *Mon. Not. R. astr. Soc.*, **178**, 81p

[31] Wang, Y.-M., & Welter, G. L., 1981, *Astr.Astrophysics.*, **102**, 97

[32] Wang, Y.-M., & Frank, J., 1981, *Astr.Astrophysics.*, **93**, 255